Acta Geochim (2021) 40(2):251–270
https://doi.org/10.1007/s11631-020-00448-w

ORIGINAL ARTICLE

Geochronology, geochemistry and Hf isotopes of andesites in the Sandaowanzi gold deposit (Great Xing'an Range, NE China): implications for petrogenesis, tectonic setting, and mineralization

Runtao Yu[1] · Bile Li[1] · Fengyue Sun[1] · Zhihua Li[1] · Huawei Li[1] · Yufan Shi[1]

Received: 15 July 2020 / Revised: 7 December 2020 / Accepted: 14 December 2020 / Published online: 4 January 2021

Abstract The Sandaowanzi gold deposit is an extremely Au-rich deposit in the Northern Great Hinggan Range in recent years. Zircon U–Pb geochronology, Hf isotope analysis, and the geochemistry of andesites of the Longjiang Formation from the Sandaowanzi gold deposit were used to investigate the origin, magmatic evolution as well as mineralization and tectonic setting of the Early Cretaceous epithermal gold deposits in the northern Great Hinggan Range area. Zircon U–Pb dating reveals an emplacement age of 123.4 ± 0.3 Ma, indicating that the andesites of the Sandaowanzi gold deposit was formed during the Early Cretaceous. The andesites are enriched in light rare earth elements relative to heavy rare earth elements and have weak negative Eu anomalies (δEu = 0.76–0.90). The rocks are also enriched in large-ion lithophile elements, such as Rb, Ba, Th, U, and K, and depleted in the high-field-strength elements, such as Nb, Ta, and P. These characteristics are typical of volcanic rocks related to subduction. Igneous zircons from the andesite samples have relatively homogeneous Hf isotope ratios, $^{176}Hf/^{177}Hf$ values of 0.282343–0.282502, εHf(t) values of − 12.58 to − 6.95, and two-stage model ages (T_{DM2}) of 1743–1431 Ma. The characteristics of the andesites of the Longjiang Formation are consistent with derivation from partial melting of enriched mantle wedge metasomatized by subducted-slab-derived fluids. These rocks formed in an extensional environment associated with the closure of the Mongol–Okhotsk Ocean and subduction of the Paleo-Pacific Plate. Mineralization occurred towards the end of volcanism, and the magmatic activity and mineralization are products of the same geodynamic setting.

Keywords Andesites of longjiang formation · Zircon U–Pb geochronology · Hf isotope · Geochemistry · Sandaowanzi gold deposit

Supplementary Information The online version of this article (https://doi.org/10.1007/s11631-020-00448-w) contains supplementary material, which is available to authorized users.

✉ Bile Li
libl@jlu.edu.cn

Runtao Yu
yurt17@mails.jlu.edu.cn

Fengyue Sun
sfy@jlu.edu.cn

Zhihua Li
lzhameame@163.com

Huawei Li
hwli17@mails.jlu.edu.cn

Yufan Shi
yfshi19@mails.jlu.edu.cn

[1] College of Earth Science, Jilin University, No. 2199 Jianshe Street, Changchun 130061, China

1 Introduction

The Sandaowanzi epithermal gold deposit in NE China is important because it is the only deposit in China that is dominated by calaverite and with extremely high gold content (the highest Au grade of the ore exceeding 1%) (Liu et al. 2011, 2013a, b; Zhai et al. 2015, 2018). The deposit is hosted in quartz veins intruding volcanic rocks of the Longjiang Formation. It has a total reserve of ≥ 28t Au with an average grade of 15 g/t and more than 95% of the gold occurs as coarse-grained telluride (Liu et al. 2011, 2013a, b; Lü 2011). The Sandaowanzi gold mining company started mining in early 2006, and ≥ 20 t of Au

has been recovered to date (Liu et al. 2011). Recent mining revealed the existence of bonanza Au and Ag telluride ores, with grades of Au, Ag, and Te up to 35,000, 25,000, and 30,000 g/t, respectively (Zhai et al. 2015, 2018).

Epithermal gold deposits are one of the most important types of gold deposits globally and they have been a subject of research since their discovery (Sillitoe 1997; Cooke and Simmons 2000; Qiu et al. 2008; Richards 2009; Chen 2010). Most epithermal gold deposits are located in one of three metallogenic domains: the circum-Pacific belt, the Mediterranean–Himalayan belt, and the Mongol–Okhotsk belt (Ying 1999; Chen et al. 2001), and are thought to have been formed from low salinity fluids at shallow depths and low temperatures in environments spatially related to crater or caldera structures (Mao et al. 2003). The location of deposits is also influenced by deep regional faults; the intersections of deep regional faults with the ring fractures of calderas are considered highly prospective (Chang and Li 2015).

Calaverite is an accessory mineral in a range of epithermal mineral deposit types (Pals and Spry 2003; Ciobanu et al. 2006; Wallier et al. 2006; Cooke 2001), but few epithermal deposits are classified as telluride gold deposits (Cook and Ciobanu, 2005). High concentrations of Calaverite are often associated with low sulfidation mineralization related to arc magmatism (Cooke and Simmons 2000; Damdinov et al. 2007; Chang and Li 2015). Telluride gold deposits are commonly associated with alkaline or sub-alkaline magmatism (Cooke and Simmons 2000; Kelley and Ludington 2002; Cook et al. 2009). However, telluride-enriched epithermal mineralization has also been reported in calc-alkaline rocks (Cook and Ciobanu 2005).

The northern Great Hinggan Range hosts the Sandaowanzi (Liu et al. 2011, 2013a, b; Zhai et al. 2015, 2018), Shabaosi (Liu et al. 2013a, b), and Baoxinggou (Zhou et al. 2018) epithermal gold deposits, and is one of the most important epithermal gold mineralization regions in China. These deposits occur in or are spatially related to, Early Cretaceous volcanic rocks (Wang et al. 2017). Large-scale volcanism occurred in the northern Great Hinggan Range during the Early Cretaceous (Zhang et al. 2010). The consensus is that the Early Cretaceous geodynamic setting of northeast China was extensional, based on metamorphic core complexes (Liu et al. 2005; Yang et al. 2007), Early Cretaceous A-type granites are closely related to Early Cretaceous volcanic rocks (Jahn et al. 2001; Wu et al. 2002; Ji et al. 2019), and the extensive development of bimodal volcanic rock assemblages (Wang et al. 2006; Zhang et al. 2010) throughout eastern China during the Early Cretaceous. However, the mechanisms that caused extension are controversial and include: (1) uplift by a mantle plume or a similar intraplate process (Lin et al. 1998; Ge et al. 1999, 2000); (2) post-orogenic extension subsequent to closure of the Mongol–Okhotsk Ocean (Fan et al. 2003; Meng 2003; Yang et al. 2015; Deng et al. 2018); (3) subduction of the Paleo-Pacific Plate beneath eastern China (Zhao et al. 1998; Wang et al. 2006; Ouyang et al. 2013; Xu et al. 2013).

In this paper, we report the results of geochemical, zircon U–Pb, and Hf isotope analysis of andesites from the Longjiang Formation, which hosts the Sandaowanzi gold deposit. The data were used to evaluate the proposed geodynamic models, reveal the magma source and tectonic setting of the Longjiang Formation, constrain its relationship to mineralization, and provide new insights into regional mineralization.

2 Regional geology

Northeast China is located in the eastern Central Asian Orogenic Belt (CAOB), which is a giant accretionary orogen bounded by the Siberian and North China cratons, by the Pacific Plate to the east and by the Mongol–Okhotsk slab to the northwest (Fig. 1a). From NW to SE, the CAOB consists of the Erguna Block, Xing'an Block, Songnen–Zhangguangcailing Block, Jiamusi Block, and Khanka Block, which are separated by major faults (Li 2006; Tang et al. 2013). The region experienced two stages of evolution. During the Paleozoic, the area was affected by the evolving Paleo-Asian Ocean tectonic system, which was characterized by the amalgamation of microcontinents and the final closure of the Paleo-Asian Ocean during the Late Paleozoic to Early Mesozoic. During the Mesozoic, the area was affected by the circum-Pacific and Mongol–Okhotsk tectonic systems (Xu et al. 2013).

The Sandaowanzi gold deposit is located in the northern Great Hinggan Range, which lies within the Xing'an and Ergun blocks (Fig. 1b). These blocks were thought to have amalgamated in the Early Paleozoic (Ge et al. 2005), but recent studies indicate that the units formed during the Paleozoic and Early Mesozoic (Zhang et al. 2018). Most of the rocks exposed in the study area are Paleozoic, Mesozoic, or Cenozoic in age. The Paleozoic units contain Upper Paleozoic continental volcanic–sedimentary rocks, which include the Silurian–Devonian Niqiuhe and Genlihe formations, and the Permian Wudaoling Formation. The Mesozoic units include the intermediate–silicic volcanic and clastic units of the Cretaceous Longjiang and Guanghua formations, which crop out in a belt oriented NE–SW.

Voluminous granitic magmatism, predominantly of I- and A-type granitoids, occurred in the Great Hinggan Range during the Mesozoic. The study area also includes small, sporadically distributed intrusions of Early Jurassic quartz diorite and monzogranite.

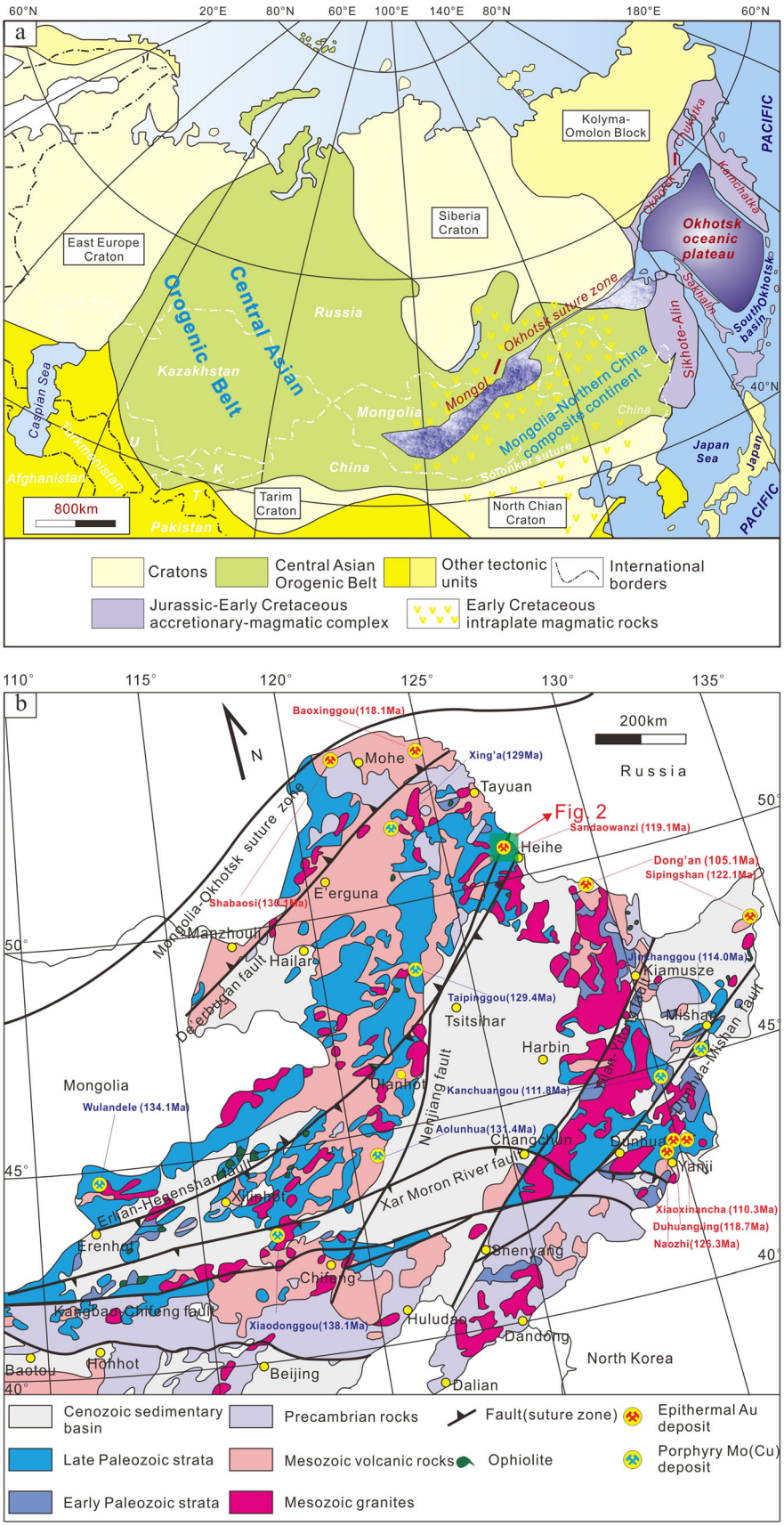

Fig. 1 **a** Location of the Central Asian Orogenic Belt (after Zhang 2014; Zhang et al. 2019), the Mongol–Okhotsk suture zone is after Halim et al. (1998) and Zorin (2016); **b** Geological map showing the distribution of epithermal and porphyry deposits in northeast China (revised after Xu et al. 2013; Deng et al. 2019). Deposit age data are from a compilation of literature data

The tectonics of the region has been controlled by the circum-Pacific and Mongol–Okhotsk tectonic systems since the Mesozoic, which generated NNE–SSW-, E–W-, and NE–SW-trending fault systems. The tectonic setting was favorable for various types of mineralization (e.g., Mo, Cu, Au), which climaxed in the Early Cretaceous and yielded a series of epithermal and porphyry deposits (Fig. 1b).

3 Ore deposit geology

The Sandaowanzi gold deposit is located in the northern Great Hinggan Range, to the north of the Northeast-East Mongolia fault basin (Fig. 2). Volcanic rocks are widespread in the Sandaowanzi ore district, and are divided into two units: the lower Longjiang Formation, which was previously thought to be the Upper Jurassic Tamulangou Formation and the upper Guanghua Formation (Lü 2011). The Longjiang Formation consists mainly of andesites, andesitic breccias, rhyolites, and tuffs. The Guanghua Formation consists of rhyolites, perlites, tuff breccias, and tuffs. The distribution of volcanic rocks within the Great Hinggan Range was controlled mainly by the existence of NE–SW- to NNE–SSW-oriented regional fault-bounded basins. On the local scale, NE–SW-oriented brittle faults offset the mineralized fractures. Northwest–SE-trending faults are mainly restricted to the Sandaowanzi mining area and are filled, in places, by Au-bearing quartz veins. A large Early Jurassic medium-grained monzogranite pluton lies unconformably below the Early Cretaceous volcanic rocks of the mining area. Post-mineralization dikes, including diabasic porphyries, rhyolitic porphyries, and dioritic porphyries, which are several tens of centimeters to several meters wide, intrude the Cretaceous volcanic rocks. Gold telluride ore occurs in quartz veins that intrude andesites of the Longjiang Formation. The orebodies are lenticular or occur within irregularly shaped quartz veins that pinch and swell along their strike and dip. There are 42 orebodies, including 21 blind orebodies, within the mining area and these form three belts that are referred to as gold ore belts I, II, and III. The metallic minerals in the ore are pyrite, chalcopyrite, sphalerite, sylvanite, and hessite (Fig. 3). The gangue minerals are quartz, plagioclase,

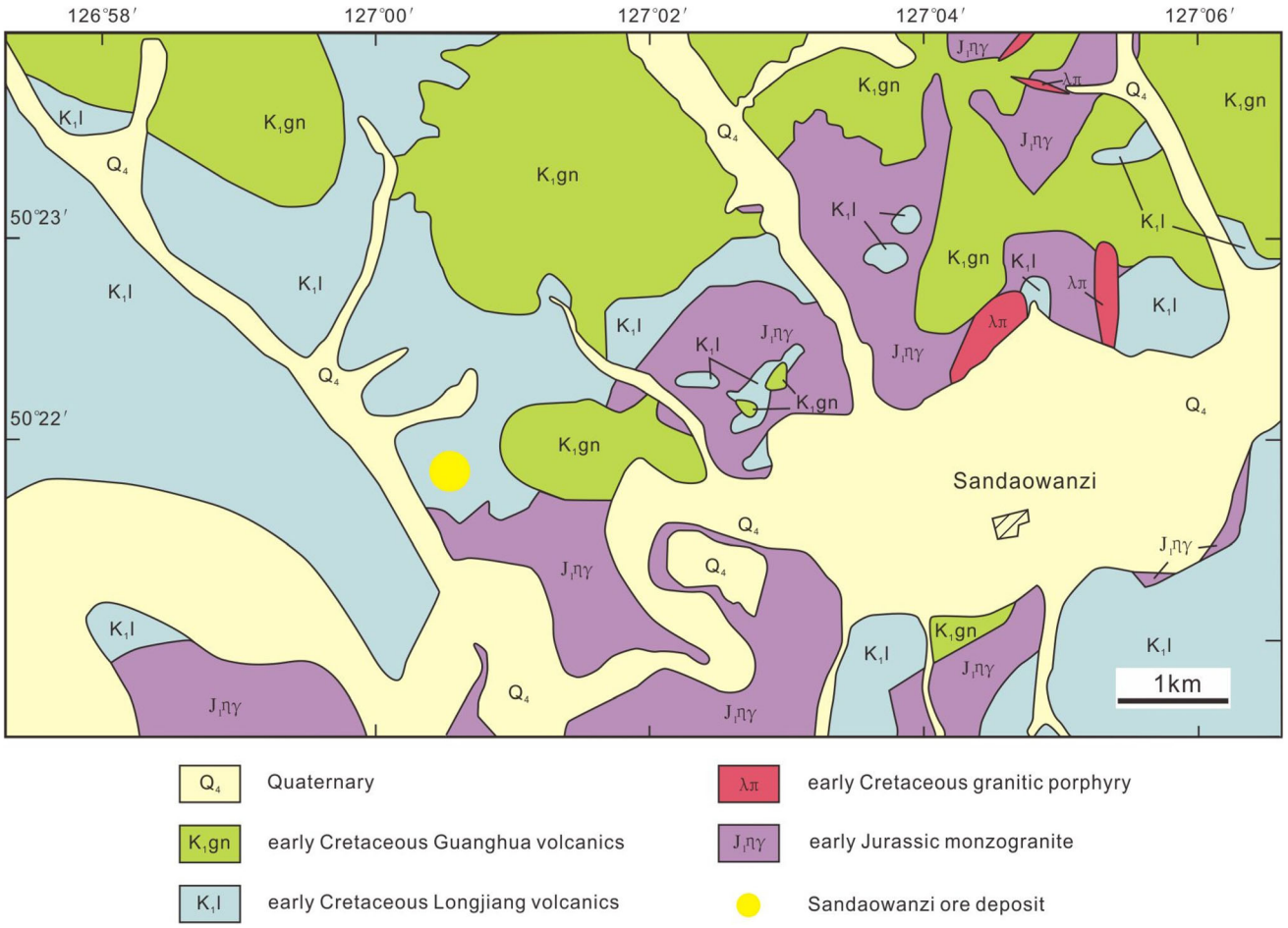

Fig. 2 Geological map of the Sandaowanzi area (revised after Wang et al. 2017)

kaolinite, sericite, chlorite, epidote, and calcite. The andesites are altered, with silicification that is particularly intense near the quartz veins. The silicification is closely related to mineralization. Volcanic rocks distal to the quartz veins have sericitised, chloritised, epidotised, and carbonated zones. These zones are banded and are asymmetrically distributed around the quartz veins.

4 Sample descriptions

The Sandaowanzi gold deposit formed during hydrothermal activity associated with the volcanism that occurred in the study area from the late Paleozoic to the end-Mesozoic rephrase. Most of the volcanic rocks in the study area formed during the Longjiang Period, but a small proportion of sporadically distributed volcanic rocks formed during the Guanghua Period. The volcanic activity caused wall rock alteration, which is common within the study area. The eight samples described in this paper are andesites of the Longjiang Formation, which were sampled from wall rock adjacent to ores within the Sandaowanzi gold deposit mining area at 50° 21′ 59″ N and 127° 00′ 07″ E. The fresh andesites are dark gray and massive, with a porphyritic texture and hyalopilitic matrix. The rocks are composed of phenocrysts (~ 35 wt%) and matrix (~ 65 wt%). The phenocrysts are mainly tabular colorless plagioclase and minor chloritization hornblende. The phenocrysts are 0.2–1.0 mm in size, and the feldspars are strongly altered to clay minerals. The matrix consists of plagioclase with small amounts of glass, quartz, and magnetite. Plagioclase in the matrix is euhedral and occurs as long tabular crystals that show a preferred orientation and occur in aggregates. The glass is interstitial to plagioclase microcrystals, defining a hyalopilitic texture in the matrix. Rare magnetite is disseminated throughout the matrix (Fig. 4).

5 Analytical methods

5.1 Zircon U–Pb geochronology

Zircons were extracted from handspci using standard magnetic and heavy-liquid separation techniques before hand-picking under a binocular microscope at the Langfang Regional Geological Survey, Hebei Province, China. All zircons were examined using transmitted and reflected light optical microscopy and their internal structures were

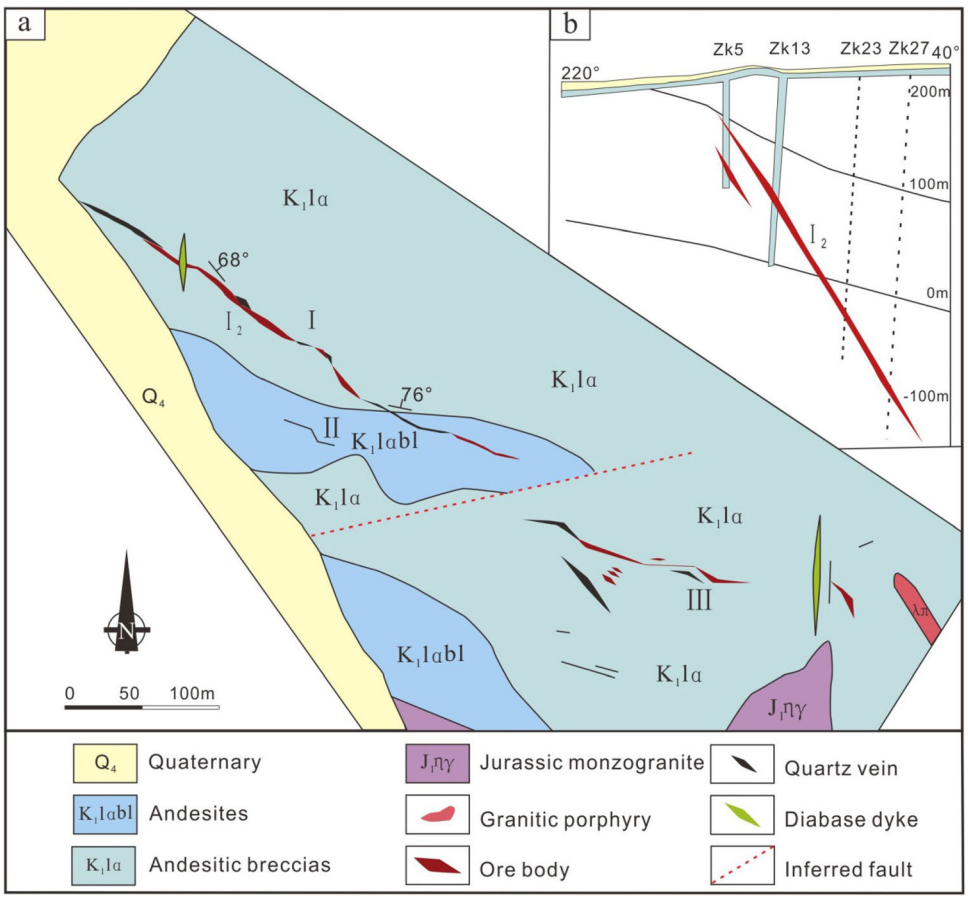

Fig. 3 **a** Geological map of the Sandaowanzi ore deposit and **b** Cross-section of the I_2 orebody (revised after Lü 2011)

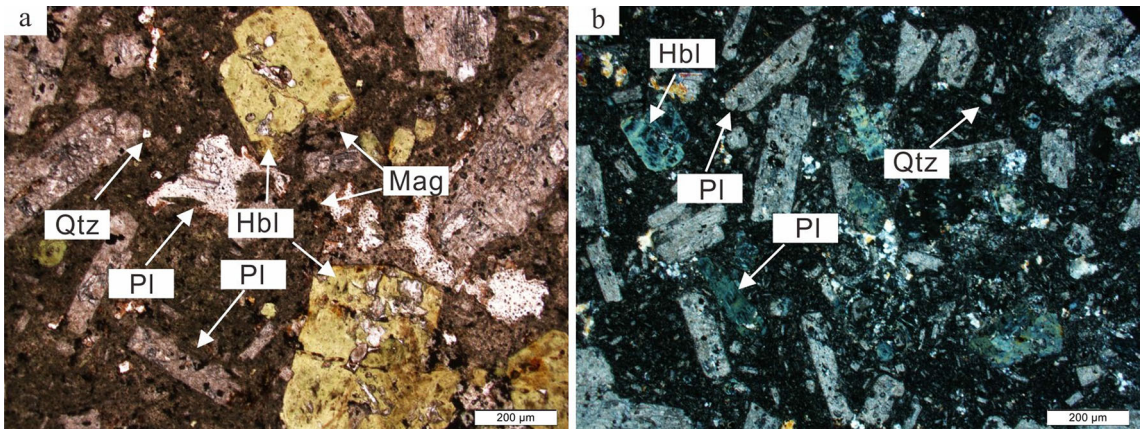

Fig. 4 Microscopic images of the andesites of Longjiang Formation in Sandaowanzi gold deposit. Mineral code: Pl, plagioclase; Qtz, quartz; Hbl, hornblende; Mag, magnetite

imaged using cathodoluminescence (CL) employing a JEOL scanning electron microscope (JEOL Ltd., Tokyo, Japan). Transparent, euhedral, non-fractured, and inclusion-free zircons were chosen for isotopic analysis. LA–ICP–MS zircon U–Pb dating was carried out at the Key Laboratory of Mineral Resources Evaluation in Northeast Asia, Ministry of Land and Resources, Jilin University, Changchun, China. The zircons were analyzed by Agilent 7900 ICP–MS instrument (Agilent Ltd., St Leonards, NSW, USA) connected to a COMPexPro102 Geolaspro 193 nm ArF Excimer laser (Coherent Inc., Santa Clara, CA, USA). Helium was used as the carrier gas. The analysis spots were 32 μm in diameter. U, Th, and Pb concentrations were calibrated using ^{29}Si as an internal standard. The zircon standard 91500 (Wiedenbeck et al. 1995) and the National Institute of Science and Technology NIST610 reference standard were used as an external standard to normalize isotopic fractionation during analysis. Uncertainties of individual analyses are reported with 1σ error. Analytical procedures used follow those described by Yuan et al. (2004), and the isotopic data were processed using the Glitter 4.0 data reduction software package. Common Pb was corrected following Andersen (2002). The analytical data were presented in U–Pb Concordia diagrams with 1σ errors and weighted mean ages were calculated at 1σ confidence level. The data were processed using the Isoplot (Version 3.0) program (Ludwig 2003).

5.2 Zircon in-situ Lu–Hf isotope analysis

In-situ zircon Hf isotopic analyses were undertaken using a Neptune-plus multicollector (MC–ICP–MS) (Thermo Electron Corporation, Madison, WI, USA) coupled to a New Wave UP213 excimer ArF laser-ablation system (Electro Scientific Industries, Inc., Portland, OR, USA), with a laser spot size of 30 μm, a laser beam energy density of 16 J/cm^2, an ablation time of 31 s and a laser pulse frequency of 8 Hz, at the MLR Key Laboratory of Metallogeny and Mineral Assessment, Institute of Mineral Resources, Chinese Academy of Geological Sciences, Beijing, China. Zircons GJ-1 were used as an external standard. The present-day chondritic radio (CHUR) of $^{176}Hf/^{177}Hf = 0.282772$ and $^{176}Lu/^{177}Hf = 0.0332$ (Blichert-Toft et al. 1999) were adopted to calculate εHf(t) values. In the calculation of Hf model ages, $^{176}Lu/^{177}Hf$ and $^{176}Hf/^{177}Hf$ were 0.0384 and 0.28325, respectively (Blichert-Toft et al. 1999). Details of the analytical techniques and data calculated using the ICP–MS Data Calsoftware were described by Wu et al. (2006).

5.3 Whole-rock major and trace elements

Eight andesites samples (Nos. SDW-Y1-Y8) were examined by petrography and collected for whole-rock analyses. Following the removal of weathered surfaces, the fresh and unaltered diorite samples were crushed, cleaned with deionized water and grounded in an agate mill to 200 mesh. All whole-rock analyses were undertaken at the Key Laboratory of Mineral Resources Evaluation in Northeast Asia, Ministry of Land and Resources, Jilin University, Changchun, China.

Major-element contents were determined by X-ray fluorescence (XRF), which was analyzed using a PW2404 instrument and fused glass disks. The loss on ignition (LOI) was acquired by the weight difference between burning and very high temperature (1000 °C). Trace-element contents were determined using an Agilent 7500a ICP–MS (Agilent Ltd., St Leonards, NSW, USA) after digestion of samples in Teflon bombs by HF-HNO_3. Standard samples for analysis were USGS (US Geological Survey standard) AGV-1 (andesite), BCR-2 (basalt), and

BHVO-1 (basalt) (Rudnick et al. 2004), which indicated that the precision and accuracy was better than 5% for major elements and 10% for trace elements. The FeO content was determined by the potassium dichromate volumetric method, which follows the standards of GB/T 14505 and GB/T 14506.1 of the People's Republic of China.

6 Results

6.1 Zircon U–Pb geochronology

CL images show that the zircons are euhedral–subhedral granular, short prismatic to long columnar, and that the grain size is ~ 50–150 μm. Oscillatory growth zoning, with variable zone width, is visible in most zircons. The crystal planes are well developed, defining prominent pyramids (Fig. 5a). The Th/U ratios are > 0.4 (0.40–1.05), typical of magmatic zircons (Hoskin and Schaltegger 2003). All 18 analyses are concordant. The $^{206}Pb/^{238}U$ data yielded a weighted-mean age of 123.3 ± 0.8 Ma (MSWD = 1.8) (Table 1) (Fig. 5b), which is within error of the concordant age123.4 ± 0.3 Ma (MSWD = 1.8) (Fig. 5c). Based on these data, the andesites of the Sandaowanzi gold deposit formed during the Early Cretaceous.

6.2 Geochemical characteristics

The andesites were altered to different extents by the hydrothermal activity and commonly occurred kaolinization and sericization in the study area. The loss-on-ignition (LOI) values of the relatively fresh samples selected for analysis are still relatively high. The samples have relatively high loss-on-ignition (LOI) values range from 2.53 to 8.90 wt%, so the possible mobilization of some elements during alteration needs to be discussed before concluding their geochemistry. All the andesites samples of this study have no pronounced Ce anomalies ($Ce/Ce_* = 1.11$ on average), indicating that they have not been significantly affected by alteration (Polat et al. 2002). In addition, there is no correlation between LOI and MgO, TiO_2, P_2O_5, Al_2O_3, $Fe_2O_3^T$, and Th content (Fig. S1), indicating the alteration may have little impact on elementary signatures. But the content of Na_2O and K_2O decreased with the increase of LOI and the content of CaO increased with the increase of LOI, indicating the migrating during the alteration process (Fig. S1). In addition, Thorium (Th) is considered to be stable during alteration, and so it was frequently used as a reference for mobilities of other trace elements (Pearce and Parkinson 1993). The samples show linear correlations between Th and Hf, La, Ta, Yb, and La, and slightly obvious correlations between Th and Sr, Sm and Rb (Fig. S2). These observations suggest that alteration processes had not significantly affect HFSEs (e.g., Nb, Hf, and Ta), REEs, and LILEs (e.g., Sr, Rb). Therefore, the HFSEs, REEs, LILEs, partial major elements (MgO, TiO_2, P_2O_5, Al_2O_3, $Fe_2O_3^T$), and compatible elements can be employed in the following discussion about the petrogenesis and source characteristics of the studied diorite samples.

6.2.1 *Major elements*

The andesite samples have moderate SiO_2 contents (47.72–61.79 wt%, average = 56.21 wt%), high total alkalis and high Na ($Na_2O + K_2O$ = 4.07–7.71 wt%, average = 5.24 wt%; Na_2O = 2.15–5.14 wt%, average = 3.46 wt%; K_2O = 1.32–2.57 wt%, average = 1.78 wt%; $Na_2O > K_2O$, Na_2O/K_2O = 1.04–3.46) (Table 2). The Rittman index, σ_{43} [$\sigma_{43} = (Na_2O + K_2O) \times (Na_2O + K_2O)/(SiO_2\text{-}43)$], is 0.88–6.71 with an average of 2.78, indicating that the rocks are calc-alkaline. The samples contain 14.71–18.42 wt% Al_2O_3 (average = 16.71 wt%), and the aluminum saturation index (A/CNK) is 0.75–1.35, indicating that the rocks are quasi-

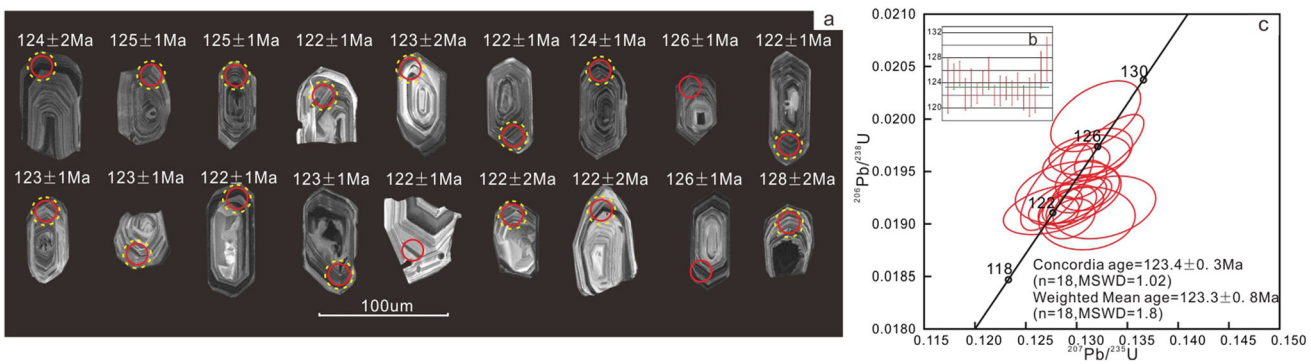

Fig. 5 Zircon CL images (**a**) weighted mean age (**b**), and the harmonious graphs of zircon U–Pb age (**c**) of the andesites of Longjiang Formation in Sandaowanzi gold deposit

Table 1 Zircon U–Pb data of the andesites of Longjiang Formation in Sandaowanzi gold deposit

Sample	Th/U	$^{207}Pb/^{206}Pb$		$^{207}Pb/^{235}U$		$^{206}Pb/^{238}U$		$^{206}Pb/^{238}U$	
		Ratio	1σ	Ratio	1σ	Ratio	1σ	t(Ma)	1σ
SDW-N1-01	0.46	0.0481	0.0010	0.1281	0.0029	0.0193	0.0003	124	2
SDW-N1-02	0.62	0.0482	0.0010	0.1300	0.0026	0.0196	0.0002	125	1
SDW-N1-03	0.65	0.0485	0.0012	0.1313	0.0033	0.0197	0.0002	125	1
SDW-N1-04	0.60	0.0482	0.0015	0.1277	0.0041	0.0191	0.0002	122	1
SDW-N1-05	0.89	0.0485	0.0016	0.1292	0.0043	0.0193	0.0002	123	2
SDW-N1-06	0.90	0.0487	0.0006	0.1286	0.0017	0.0192	0.0001	122	1
SDW-N1-07	0.74	0.0488	0.0008	0.1304	0.0021	0.0194	0.0001	124	1
SDW-N1-08	0.40	0.0487	0.0010	0.1320	0.0030	0.0197	0.0002	126	1
SDW-N1-09	1.01	0.0486	0.0006	0.1282	0.0017	0.0191	0.0001	122	1
SDW-N1-10	0.54	0.0487	0.0011	0.1294	0.0033	0.0192	0.0002	123	1
SDW-N1-11	0.61	0.0490	0.0008	0.1303	0.0022	0.0193	0.0001	123	1
SDW-N1-12	0.85	0.0489	0.0007	0.1295	0.0020	0.0192	0.0002	122	1
SDW-N1-13	0.54	0.0493	0.0009	0.1312	0.0025	0.0193	0.0002	123	1
SDW-N1-14	0.92	0.0494	0.0008	0.1294	0.0021	0.0190	0.0002	122	1
SDW-N1-15	1.05	0.0501	0.0016	0.1311	0.0039	0.0191	0.0002	122	2
SDW-N1-16	0.97	0.0502	0.0016	0.1327	0.0042	0.0192	0.0002	122	2
SDW-N1-17	1.03	0.0487	0.0009	0.1332	0.0029	0.0197	0.0002	126	1
SDW-N1-18	0.77	0.0478	0.0013	0.1320	0.0036	0.0200	0.0003	128	2

aluminous to peraluminous. The TiO_2 content is 0.65–0.85 wt% (average = 0.73 wt%), the MgO content is 1.86–4.46 wt% (average = 3.44 wt%), and the $Mg^{\#}$ values are high (41.25–58.37, average = 52.94). The samples are Al-rich ($Al_2O_3 > K_2O + Na_2O + CaO$) and alkali-rich.

The andesites were altered to different extents by the hydrothermal activity in the study area, and so the loss on ignition values are relatively high. The high-field-strength elements (HFSEs), which are relatively unaffected by metamorphism, alteration, and weathering, were used to classify and discriminate among the altered volcanic rocks. Most of the rocks plot within the andesite field of Pearce and Peate (1995) on a Zr/TiO_2 versus Nb/Y diagram (Fig. 6a), and most of the andesites plot within the calc-alkaline field on a Th versus Co diagram (Hastie et al. 2007), except two samples, which are classified as high-K andesite and a shoshonite (Fig. 6b).

6.2.2 Trace elements

The REE concentrations were normalized to chondrite values (Boynton 1984). The andesite samples have relatively low total REEs (110.71×10^{-6}–141.02×10^{-6}, average = 123.81×10^{-6} (Table 2). The total concentration of the light REEs (ΣLREE) is 99.96×10^{-6}–127.79×10^{-6} (average = 112.65×10^{-6}) and the total concentration of the heavy REEs (ΣHREE) is 10.59×10^{-6}–11.96×10^{-6} (average = 11.16×10^{-6}). The chondrite-normalized REE patterns show similar trends, consistent with a single magma source and similar magma evolution, and are generally LREE enriched (Fig. 7a). The chondrite-normalized La/Yb value ($(La/Yb)_N$) is 8.28–12.86 (average = 10.38) and the LREE/HREE ratio is 9.11–11.56 (average = 10.10), indicating that these rocks are significantly enriched in light REEs (LREE), strongly depleted in heavy REEs (HREE) and strong fractionation between the LREEs and the HREEs. The $(La/Sm)_N$ values are 2.91–3.78 (average = 3.33), indicating fractionation of the LREEs. The $(Gd/Yb)_N$ values are 1.70–2.07 (average = 1.87), indicating that the HREEs are not significantly fractionated from each other. The andesites have weak negative Eu anomalies (0.76–0.90, average = 0.84).

The trace element data were normalized to a primitive mantle (Sun and McDonough 1989). The Ba and Sr contents are high (459.65×10^{-6}–908.98×10^{-6} and 434.46×10^{-6}–855.58×10^{-6}, respectively) and Rb contents are low (17.80×10^{-6}–61.80×10^{-6}) (Table 2). On a primitive-mantle-normalized trace element diagram, the samples are enriched in large-ion lithophile elements (LILEs; e.g., Rb, Ba, Th, U, and K) and depleted in HFSEs (e.g., Nb, Ta, and P) relative to the primitive mantle (Fig. 7b). These characteristics are typical of volcanic rocks related to subduction (Condie 2015) (Fig. 8).

6.3 Zircon in-situ Lu–Hf isotope results

In-situ zircon Hf isotope analysis was performed at 15 of the 18 positions chosen for U–Pb dating (Table 2). The

Table 2 Major (wt%) and trace elements ($\times 10^{-6}$) compositions of the andesites of Longjiang Formation in Sandaowanzi gold deposit

Sample	SDW-Y1	SDW-Y2	SDW-Y3	SDW-Y4	SDW-Y5	SDW-Y6	SDW-Y7	SDW-Y8
SiO_2	60.67	53.50	50.34	58.20	47.72	61.79	60.22	57.27
TiO_2	0.69	0.85	0.77	0.77	0.78	0.65	0.66	0.65
Al_2O_3	17.17	18.16	18.42	17.15	18.37	14.74	14.93	14.71
$Fe_2O_3^T$	5.26	7.12	6.41	6.75	6.30	4.91	5.17	5.22
MnO	0.12	0.11	0.11	0.09	0.12	0.11	0.13	0.14
MgO	1.86	4.29	4.11	4.17	4.46	2.80	2.91	2.95
CaO	3.35	4.74	6.66	2.88	7.69	5.05	5.58	7.56
Na_2O	5.14	3.91	4.58	3.59	3.98	2.15	2.12	2.23
K_2O	2.57	1.33	1.32	1.45	1.65	1.92	2.04	1.93
P_2O_5	0.27	0.25	0.24	0.23	0.24	0.22	0.21	0.21
LOI	2.53	6.38	7.66	4.96	8.90	6.14	6.54	7.71
Total	99.67	100.67	100.65	100.31	100.23	100.58	100.61	100.65
σ43	3.37	2.62	4.75	1.67	6.71	0.88	1.01	1.21
A/CNK	0.99	1.10	0.87	1.35	0.82	0.99	0.94	0.75
$Mg^{\#}$	41.25	52.72	52.79	52.99	54.45	55.02	55.94	58.37
Li	26.17	45.08	41.22	40.41	44.31	38.67	41.75	41.57
Be	2.54	2.59	1.99	2.21	2.25	1.93	2.03	1.84
Sc	12.72	19.78	17.77	16.86	18.41	16.02	16.14	16.42
V	98.61	141.83	126.03	117.32	129.28	81.39	88.85	99.45
Cr	8.12	163.15	147.38	196.59	130.08	82.19	95.38	89.00
Co	14.48	28.66	27.08	28.89	24.70	17.53	17.65	18.39
Ni	7.78	45.27	47.07	53.40	38.53	27.49	28.13	28.95
Cu	17.83	21.68	24.68	33.84	31.91	32.26	22.69	21.38
Zn	117.90	132.15	111.16	113.89	113.45	81.26	80.71	76.92
Ga	21.26	20.32	19.50	18.03	19.30	15.77	16.21	16.28
As	2.72	1.21	0.97	1.10	1.11	1.48	1.54	1.63
Rb	61.80	28.94	17.80	29.34	38.95	62.31	58.32	58.75
Sr	855.58	669.40	644.21	518.56	657.43	434.96	434.46	442.26
Y	14.25	16.47	14.73	13.55	15.36	13.73	13.43	13.76
Zr	163.46	156.95	146.34	142.20	149.58	129.03	129.10	127.66
Nb	7.08	6.50	6.49	5.96	6.59	5.10	5.20	5.21
Mo	0.57	0.19	0.16	0.15	0.12	0.30	0.16	0.18
Cd	0.33	0.10	0.10	0.09	0.11	0.09	0.11	0.10
In	0.03	0.04	0.04	0.04	0.04	0.03	0.03	0.03
Cs	6.08	2.58	1.92	2.83	3.91	6.36	6.70	6.04
Ba	908.98	508.39	462.48	459.65	470.73	589.88	683.73	510.85
La	28.81	24.56	20.26	20.71	24.06	24.11	22.27	26.64
Ce	61.07	54.14	49.38	47.58	51.79	54.20	49.54	58.37
Pr	6.30	5.71	5.12	4.94	5.70	5.57	5.28	5.98
Nd	27.57	24.65	22.57	21.61	24.62	24.03	23.10	25.99
Sm	4.79	4.67	4.38	4.16	4.69	4.44	4.18	4.76
Eu	1.25	1.11	1.12	0.96	1.22	0.99	1.01	1.24
Gd	3.77	3.79	3.48	3.33	3.75	3.56	3.41	3.74
Tb	0.58	0.63	0.56	0.53	0.61	0.57	0.55	0.58
Dy	2.76	2.80	2.90	2.74	2.78	2.66	2.69	2.77
Ho	0.54	0.62	0.56	0.53	0.58	0.52	0.51	0.52
Er	1.65	1.88	1.70	1.61	1.80	1.60	1.59	1.60
Tm	0.21	0.24	0.22	0.22	0.23	0.19	0.20	0.19

Table 2 continued

Sample	SDW-Y1	SDW-Y2	SDW-Y3	SDW-Y4	SDW-Y5	SDW-Y6	SDW-Y7	SDW-Y8
Yb	1.51	1.75	1.65	1.57	1.69	1.44	1.45	1.46
Lu	0.21	0.25	0.22	0.22	0.24	0.20	0.19	0.19
Hf	4.34	4.16	3.97	3.85	4.07	3.69	3.64	3.64
Ta	0.40	0.37	0.35	0.33	0.36	0.29	0.29	0.29
W	0.63	0.41	0.42	0.36	0.59	0.63	0.61	0.55
Tl	0.45	0.14	0.15	0.18	0.31	0.34	0.36	0.35
Pb	19.41	18.07	18.60	16.40	17.84	17.22	18.67	17.78
Bi	0.08	0.09	0.03	0.05	0.04	0.06	0.07	0.06
Th	6.96	5.83	5.03	5.22	5.40	5.66	5.37	5.44
U	1.88	1.95	1.75	1.76	1.67	1.69	1.57	1.65
ΣREE	141.02	126.80	114.12	110.71	123.76	124.08	115.97	134.03
LREE	129.79	114.84	102.83	99.96	112.08	113.34	105.38	122.98
HREE	11.23	11.96	11.29	10.75	11.68	10.74	10.59	11.05
(La/Sm)N	3.78	3.31	2.91	3.13	3.23	3.42	3.35	3.52
(Gd/Yb)N	1.70	1.71	1.75	1.79	1.90	1.99	2.01	2.07
(La/Yb)N	12.86	9.46	8.28	8.89	9.60	11.29	10.35	12.30
LREE/HREE	11.56	9.60	9.11	9.30	9.60	10.55	9.95	11.13
δCe	1.09	1.10	1.17	1.13	1.06	1.13	1.10	1.11
δEu	0.90	0.81	0.88	0.79	0.89	0.76	0.82	0.90

LOI, loss on ignition, $Mg^{\#}$, $100 \times Mg^{2+}/(Mg^{2+} + TFe^{2+})$, A/CNK = mole $Al_2O_3/(CaO + Na_2O + K_2O)$, $\sigma 43 = (Na_2O + K_2O) \times (Na_2O + K_2O)/(SiO_2\text{-}43)$

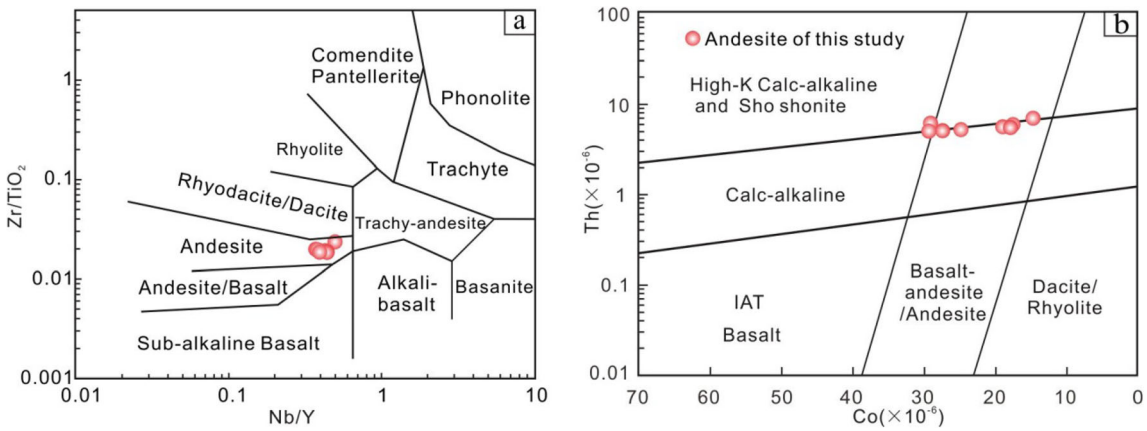

Fig. 6 Geochemical classification: **a** Zr/Ti versus Nb/Y classification diagram (after Pearce and Peate 1995); **b** classification of high-K/shoshonite andesites and calc-alkaline granitoids in Th versus Co diagram (after Hastie et al. 2007)

zircons have relatively homogeneous Hf isotopic compositions, with $^{176}Hf/^{177}Hf$ ratios of 0.282343–0.282502 calculated at the inferred time of formation (123 Ma). The εHf(t) values are − 12.58 to − 6.95, the single-stage model ages (T_{DM1}) are 1295–1057 Ma, and the two-stage model ages (T_{DM2}) are 1743–1431 Ma.

7 Discussion

7.1 Magma source and petrogenesis

The major and trace element and isotopic characteristics of the andesites from the study area are relatively homogenous, which indicates that they were derived from a single

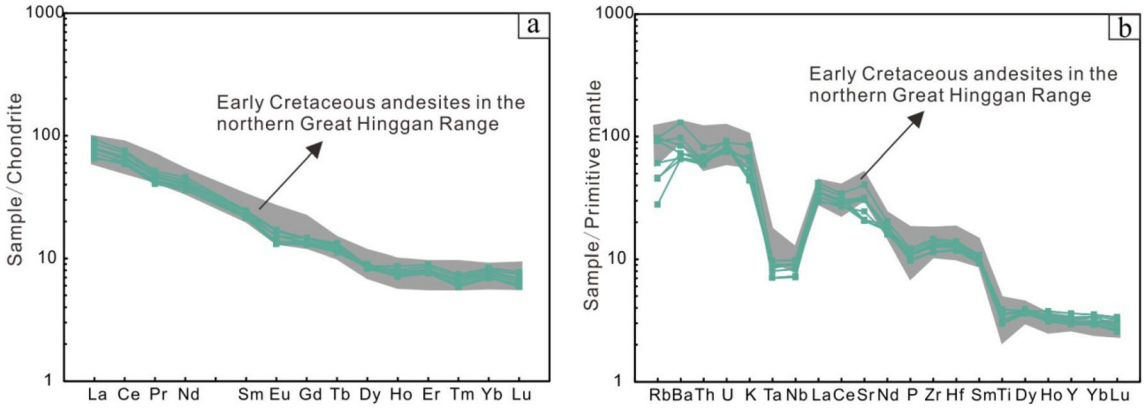

Fig. 7 REE chondrite-normalized pattern (**a**) and primitive mantle-normalized trace element spidergram (**b**) of the andesites of Longjiang Formation in Sandaowanzi gold deposit. Gray shadow areas are from a compilation of literature data (Fan et al. 2003; Li et al. 2013; Liu et al. 2018)

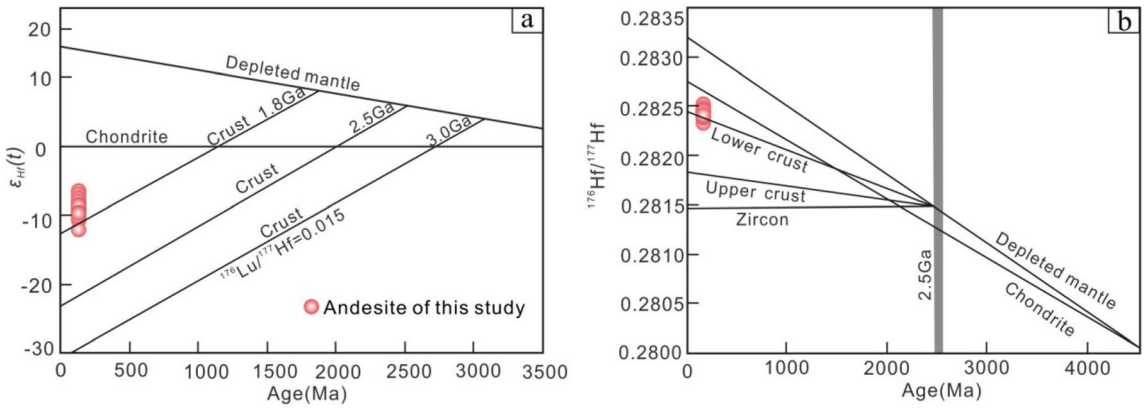

Fig. 8 Zircon Hf isotopic features for the andesites of Longjiang Formation in Sandaowanzi gold deposit (after Yang et al. 2006)

source. Generally, the $Mg^{\#}$ ($100 \times Mg^{2+}/(Mg^{2+} + TFe^{2+})$ of a mantle-derived rock ($Mg^{\#} > 40$) is higher than that of a rock formed by partial melting of the basaltic lower crust ($Mg^{\#} < 40$; Rapp and Watson 1995). The andesites of the study area have relatively low SiO_2 and high $Mg^{\#}$ numbers (average = 53), indicating an affinity to the lithospheric mantle rather than crustal material (Yang et al. 2006; Tang et al. 2009). The Nb/Ta ratios of mantle-derived magmas are relatively high (17.5 ± 2.0), while those of crust-derived magmas are relatively low (11–12) (Green 1995). The Nb/Ta ratio of the andesite samples is 17.56–18.54, consistent with a mantle source. The Rb/Sr ratio of the andesite samples is 0.03–0.14 (average = 0.08). This is close to the upper mantle value (0.034) and much lower than the average crustal value (0.35) (Taylor and Mclennan 1995). The andesite samples generally exhibit high Mg# values, high Nb/Ta ratio, and low Rb/Sr ratio, precluding the possibility that they are derived from the partial melting of the lower crust and indicating a mantle-derived magmatic source.

The mantle-derived magma may have experienced some degree of crustal contamination during ascent or residence within crustal magma chambers (Jahn et al. 1999). The Nb/U ratio and Ce/Pb are good indicators of crustal contamination (Quan et al. 2020). The samples display Nb/U (3.02–3.95) and Ce/Pb (2.65–3.28) ratios that are significantly lower than those of oceanic basalt average derived from the lithospheric mantle (Nb/U = 47 and Ce/Pb = 27; Hofmann et al. 1986), confirming the addition of a crustal component. However, the andesites have La/Nb ratios (3.12–5.11), which are significantly higher than those of continental crust in eastern China (average = 1.7; Yang et al. 2014). On a Ba/Nb–La/Nb diagram, all the andesites samples fall in the range of arc volcanic rocks (Fig. 12a), much higher than the continental crust composition. These samples display no significant correlation in the Th/La versus SiO_2, U/Nb versus SiO_2, Th/Zr versus Ce/Pb, and La/Yb versus Nb/Ta diagrams (Fig. 9a–d). These lines of evidence indicate that the mantle-derived magma was slightly contaminated by crustal materials during upwelling.

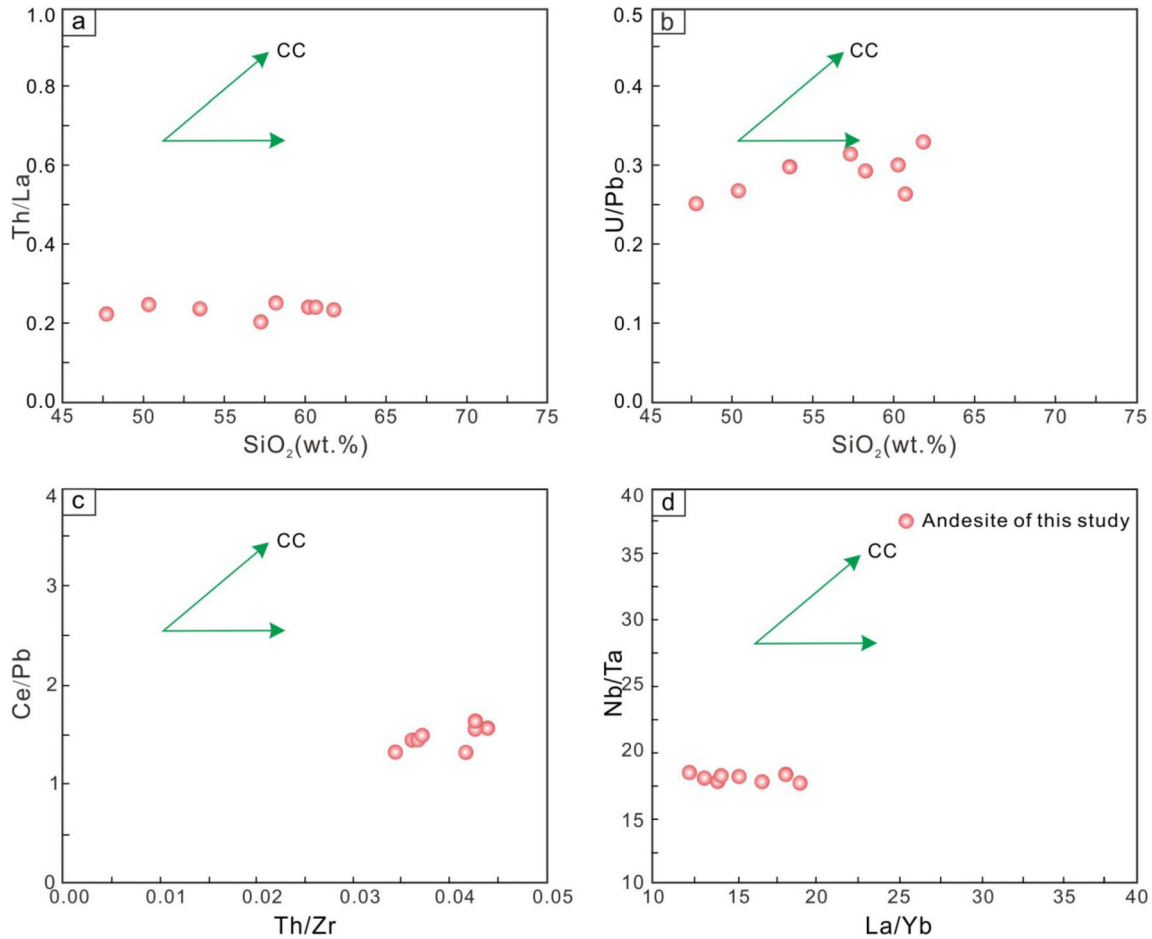

Fig. 9 **a** Th/La-SiO_2 and **b** U/Nb-SiO_2 diagrams (Ma et al. 2015), **c** Th/Zr–Ce/Pb and **d** La/Yb–Nb/Ta diagrams (Deng et al. 2018) of the andesites of Longjiang Formation in Sandaowanzi gold deposit. CC, crustal contamination

The concentrations of the compatible elements (e.g., Cr and Ni) are lower than expected for a primary basaltic magma, and so the andesites are likely to have fractionated minerals as they evolved (Atherton and Petford 1993). The trend of the data on a Cr versus Ni diagram is consistent with the fractionation of clinopyroxene (Fig. 10a). The volcanic rocks of the Longjiang Formation in the study area are enriched in the LREEs, depleted in the HREEs, and weak Eu anomalies (0.76–0.89), indicating that the magmatic evolution involved slightly fractional crystallization of plagioclase (Kazimoto and Ikingura 2014). The relatively high Sr contents of the andesites and the systematic variation trends between transition metal elements (i.e., V and Sc) indicate that the hornblende is potential fractionating mineral phases (Fig. 10b). Geochemical modeling using highly and moderately incompatible elements is an effective method to discriminate the magmatic processes of the andesites. However, in the La/Sm-La and Nb/Sm-Nb (after Schiano et al. 2010) plots, most samples define oblique straight lines (Fig. 11a, b), indicating that the rocks were not mainly derived by fractional crystallization and primarily controlled by partial melting.

The LILE enrichment and HFSE depletion of the andesites are consistent with the characteristics of subduction-related igneous rocks. Two models have been proposed to explain the distinctive geochemical features of andesites: (1) rutile and other minerals enriched in the HFSEs were residual and remained in the magma source (Ionov et al. 1999); and (2) metasomatism of the subduction-related fluids or melts in the mantle sources (Gill 1981; Grove and Kinzler 1986; Arculus 1994; Schiano et al. 2000). Rutile and hornblende are enriched in Nb and Ta, while the presence of residual rutile in the source region during magma formation would have resulted in depletion in Zr, Hf, and other elements at the same time (Ionov et al. 1999). However, although andesite samples have lower Nb and Ta values, no loss of elements such as Zr and Hf, precluding the possibility that rutile and other minerals were retained in the magma source. We, therefore, favor a model of partial melting of a mantle wedge that was metasomatized by subduction-related derived

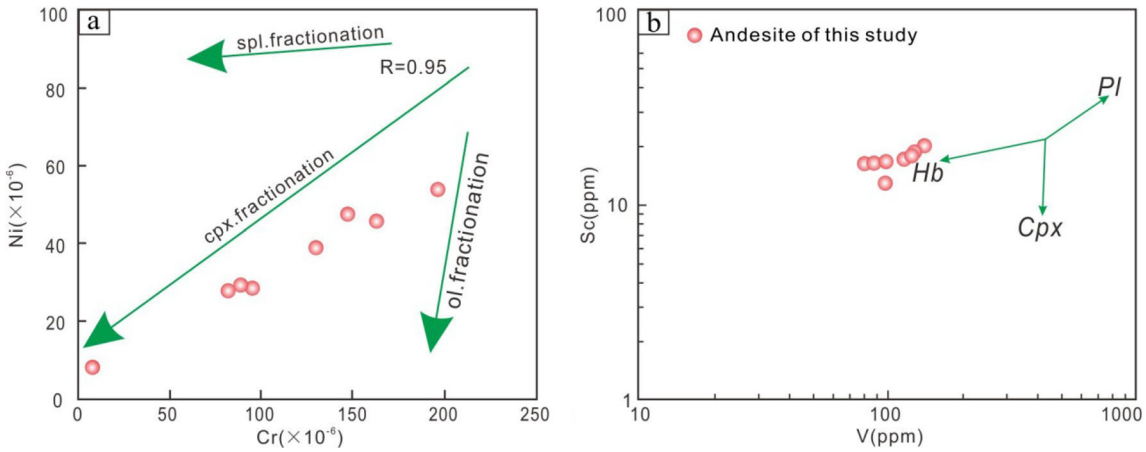

Fig. 10 **a** Ni versus Cr classification diagram and **b** Sc versus V diagram (after Sun et al. 2020) Mineral code: Pl, plagioclase; Cpx, clinopyroxene; Hbl, hornblende; Ol, Olivine; Spl, spinel

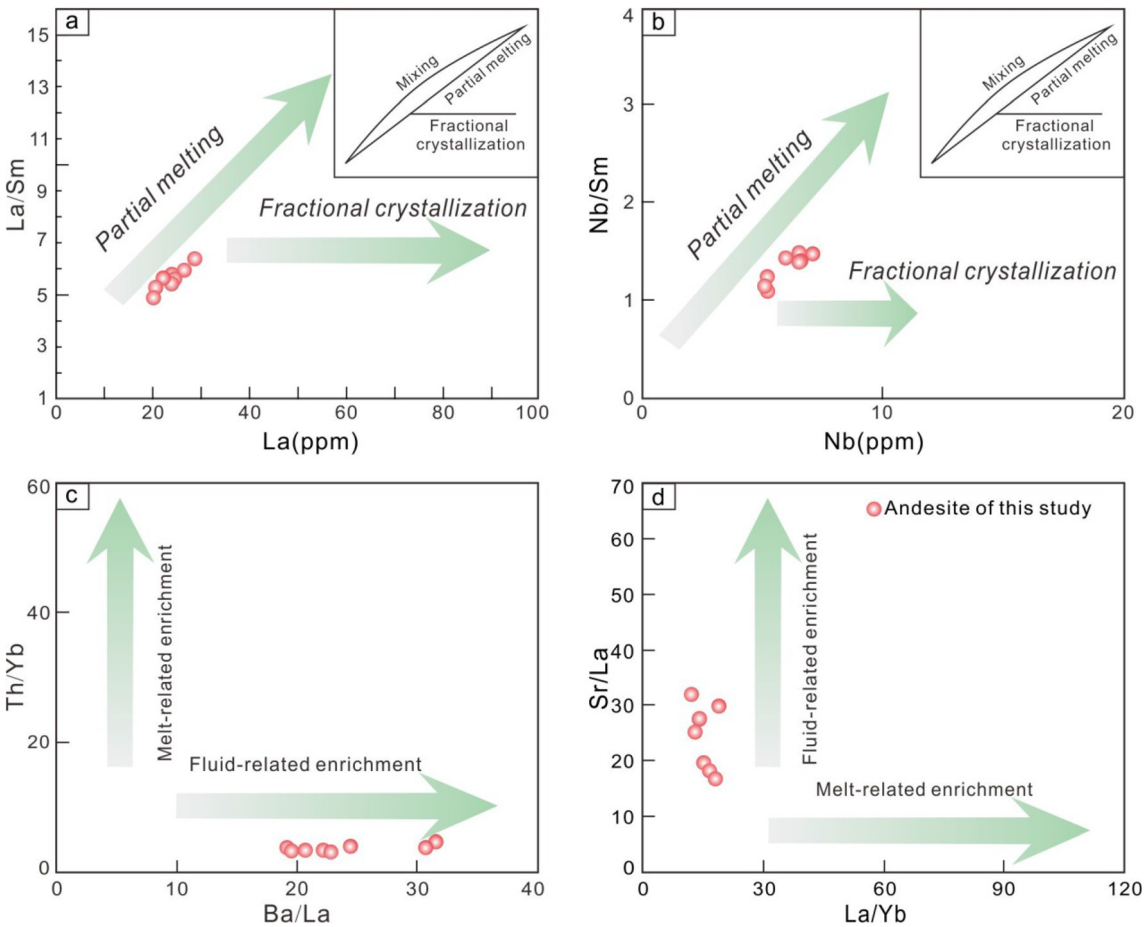

Fig. 11 **a** La/Sm versus La and Nb/Sm versus Nb diagram (after Schiano et al. 2010); **c** Th/Yb–Ba/La and **b** Sr/La–La/Yb discrimination diagrams (after Kirchenbaur et al. 2012)

fluids or melts. The Nb content of intermediate–basic magma formed by slab-derived-melt metasomatism is usually high (Yang et al. 2019), which is inconsistent with the low Nb content (5.10×10^{-6}–7.08×10^{-6}) and the negative Nb anomalies of the Sandaowanzi andesites. Therefore, the Andesites were unlikely to have been formed by metasomatized melt, and interaction between slab-derived fluids and mantle wedge was important in the

petrogenesis of the Andesites. It is supported by the result that the samples display trends characteristic of fluid-related rather than melt-related enrichment in the Th/Yb–Ba/La and Sr/La–La/Yb discrimination diagrams (Fig. 11c, d). As mentioned above, the samples show a weak fractional crystallization of plagioclase, which also proves a fluids-enriched environment in the magma source (Yuan et al. 2009).

In addition, the subduction-related igneous rocks were considered to be derived from the enriched mantle (Tatsumi et al. 1986; Hawkesworth et al. 1991), which is compatible with the Hf isotopic characteristics of the andesites of the Longjiang Formation in the Sandaowanzi gold deposit. The results of in-situ Hf isotope analysis of the andesites show $^{176}Hf/^{177}Hf$ ratios ranging from 0.282343–0.282502, and the zircon εHf(t) values show negative εHf(t) values varying from − 12.58 to − 6.95 (Fig. 8), suggesting that the parental magmas were derived from enriched mantle source (Griffin et al. 2002; Wu et al. 2007).

In summary, the geochemical characteristics and Hf isotope signatures of volcanic rocks from the Longjiang Formation, and previously reported data, indicate that the volcanic rocks of the study area were sourced from partial melting of enriched mantle wedge metasomatized by subducted-slab-derived fluids.

Previous studies found that the Sandaowanzi ore-bearing andesite had similar geochemical characteristics with gold-bearing andesite of the epithermal gold deposits in the Northern Great Hinggan Range and Eastern Jilin and Heilongjiang province, i.e., the Shangmachang gold deposit (Gao et al. 2018), the Dapingnanshan gold deposit (Shao 2017), the Tuoniuhe gold deposit (Shao 2017), the Gaosongshan gold deposit (Liu et al. 2020) and Ciweigou gold deposit (Zou 2015), suggesting these volcanic rocks were derived from a possible source region, what was considered to be mantle wedge metasomatized by subducted-slab-derived fluids. Shao (2017) measured the Au content of volcanic rock samples in the Heihe area and the result shows that the gold geochemical background content of andesite series is higher than that of other series rocks, indicating the formation of gold deposits in the study area are closely related to the Early Cretaceous andesitic volcanic rocks and the andesitic volcanic rocks may provide some material sources for the regional gold mineralization. During the process of subducted-slab-derived fluids metasomatized mantle wedge, the content of Au in magma increased continuously, which provided the material source for the continuous enrichment of Au. The Early Cretaceous volcanic rocks were formed after the eruption of this Au-rich magma, which was mineralized after hydrothermal alteration/metasomatism.

7.2 Tectonic setting and metallogenic implications

There is consensus that northeast China underwent extension during the Early Cretaceous, based on the presence of metamorphic core complexes (Liu et al. 2005; Yang et al. 2007), Early Cretaceous A-type granites that are closely related to Early Cretaceous volcanic rocks (Jahn et al. 2001; Wu et al. 2002; Ji et al. 2019), and widespread Early Cretaceous bimodal volcanism (Wang et al. 2006; Zhang et al. 2010) in eastern China. The Early Cretaceous volcanic rocks of the Great Hinggan Range formed in this extensional setting, which has been explained by (1) mantle plume uplift or similar intraplate processes (Lin et al. 1998; Ge et al. 1999, 2000); (2) closure of the Mongol–Okhotsk Ocean and subsequent post-orogenic extension (Fan et al. 2003; Meng 2003; Yang et al. 2015; Deng et al. 2018); (3) subduction of the Paleo-Pacific Plate beneath eastern China (Zhao et al. 1998; Wang et al. 2006; Ouyang et al. 2013; Xu et al. 2013).

Mantle plumes are characterized by annular zones of volcanic rocks, which were not observed in the study area (Fan et al. 2003). The Early Cretaceous volcanic rocks of the study area occur in a belt that extends the length of the Great Hinggan Range and extends into eastern China. Magmatic activity occurred from 185 to 105 Ma (Zhang et al. 2010). These characteristics are not consistent with the presence of a mantle plume.

Several lines of evidence indicate the subduction of the Paleo-Pacific Plate beneath eastern China. (1) The Early Cretaceous volcanic rocks of northeast China and surrounding areas are distributed in a belt parallel to the NNE–SSW-oriented Asian continental margin (Zhang et al. 2010). (2) Geophysical data support the existence of a high-velocity zone beneath eastern China, and this has been interpreted as a subducted oceanic crust (Huang and Zhao 2006). (3) Cretaceous accretionary complexes are common within the Asian continental margin (Liu et al. 2005; Yang et al. 2007). However, the above discussion about the subduction of the Paleo-Pacific Plate mainly involves the whole of Northeastern China, for different regions, such as the northern Great Hinggan Range and the Eastern Jilin–Heilongjiang provinces, the tectonic regime may be different. In the Early Cretaceous, large-scale volcanic rocks that erupted in the west part of the Songliao Basin, corresponding to the east part of the Songliao Basin adjacent to the Paleo-Pacific were limited (Zhang et al. 2008, 2010; Deng et al. 2018). Moreover, the mineralization age of the Early Cretaceous epithermal deposits in Northeast China shows an eastward trend of younger ages (Fig. 1b), correlating well with the spatiotemporal distribution pattern of Early Cretaceous granitoids and volcanic rocks (Zhang et al. 2010; Ouyang et al. 2013), i.e., the Shabaosi gold deposit (130.1 ± 1.3 Ma) (Liu et al. 2013a, b),

Baoxinggou gold deposit (124.9 ± 1.3 Ma) (Zhou et al. 2018) and the Beidagou gold deposit (115.5 ± 4.4 Ma) (Gao et al. 2018), which are consistent with the peak age of magmatism in the northern Great Hinggan Range and the Xiaoxinancha gold deposit (110.3 ± 1.5 Ma) (Zeng et al. 2016), the Dongan gold deposit (105.1 ± 0.7 Ma) (Zhi et al. 2016), and the Gaosongshan gold deposit (98 ± 1.6 Ma) (Liu et al. 2020), which are consistent with the peak age of magmatism in Eastern Jilin and Heilongjiang provinces. The temporal and spatial distribution of the volcanic rocks and the epithermal deposits implies that the Early Cretaceous volcanic rocks of the northern Great Hinggan Range were not only dominated by the subduction of the Pacific plate, but also by other tectonism.

Previous studies have shown that the tectonic evolution of the Mongolia Okhotsk ocean lasted from Late Paleozoic to Early Cretaceous (Zorin 2016; Tomurtogoo et al. 2005; Zhang 2014; Zhang et al. 2019). The southward subduction of the Mongol–Okhotsk ocean is generally considered to have initiated in the Late Permian (Tomurtogoo et al. 2005; Ouyang et al. 2013; Tang et al. 2013) and the final closure of the Mongolia–Okhotsk ocean may have occurred during the Late Jurassic to Early Cretaceous (Fan et al. 2003; Meng 2003; Yang et al. 2015; Deng et al. 2018). Xu et al. (2013) suggested that the influencing spatial extent of the Mongol–Okhotsk tectonic system in the Mesozoic mainly distributed in west of the Songliao basin (e.g., northern Great Hinggan Range). In the early Cretaceous, with the continuous subduction of the paleo Pacific plate, the intensity of the action in the Northern Great Hinggan Range was far less than that in the Eastern Jilin and Heilongjiang provinces. In the late early Cretaceous, the mineralization of epithermal deposits related to the subduction of the Pacific plate in the Eastern Jilin and Heilongjiang provinces broke out greatly but weakened obviously in Northern Great Hinggan Range. The above phenomenon was possibly triggered by the closure of the Mongol–Okhotsk Ocean which inhibited the westward movement of the Paleo-Pacific Oceanic plate, causing delamination of the thickened lithosphere and its gradual eastward extension (e.g., Wang et al. 2006; Ouyang et al. 2013). Regarding the impacts between the Paleo-Pacific and the Mongolia–Okhotsk tectonism on the Northern Great Hinggan Range during Early Cretaceous, we, therefore, favor a model of a superposition extensional setting of two tectonic regimes. Considering the fact that the study area is closer to the Mongol–Okhotsk suture zone than the plate boundaries of the Paleo-Pacific, the influence of the closure of the Mongol–Okhotsk Ocean was more significant in the Early Cretaceous. This conclusion can also be supported by the distribution of the data on La/Nb versus Ba/Nb (Jahn et al. 1999) and Ta/Yb versus Th/Yb diagrams (Pearce 2008). On a Ba/Nb–La/Nb diagram, all the andesites samples fall in the range of arc volcanic rocks (Fig. 12a), and on a Ta/Yb versus Th/Yb diagram, most of the andesites samples fall in the range of continental margin arc (Fig. 12b). Therefore, the rocks have the attributes of continental margin arc rocks related to the combination of post-orogenic extension after the closure of the Mongol–Okhotsk Ocean and back-arc extension caused by the subduction of the Western Pacific plate.

The type, age, and other characteristics of an ore deposit constrain its tectonic setting. Epithermal deposits are most commonly developed on the hanging wall of subduction zones on continental margins, within island arcs, and within back-arc tensile fracture belts (Cooke 2001; Kelley and Ludington 2002; Cook et al. 2009). The precise locations are controlled by the presence of volcanic edifices and deep faults. Mineralization occurred during the latter stages of volcanism (Ying 1999; Chen et al. 2001; Mao et al. 2003). The U–Pb age of zircons from andesites of the Longjiang Formation, which host the Sandaowanzi gold deposit, is 123.3 ± 0.8 Ma, close to the Rb–Sr age of hydrothermal pyrite from the Sandaowanzi gold deposit (119.1 ± 3.9 Ma) (Zhai et al. 2015). Therefore, volcanism and mineralization occurred late in the Early Cretaceous, and mineralization occurred slightly later than the formation of the volcanic host rocks. Other epithermal gold deposits, including the Shabaosi gold deposit (130.1 ± 1.3 Ma) (Liu et al. 2013a, b) and Baoxinggou gold deposit (124.9 ± 1.3 Ma) (Zhou et al. 2018), formed in northeast China at this time are also linked to volcanic activity in the late Early Cretaceous. The volcanoes and the epithermal deposits formed at similar times and are spatially distributed in an arc-shaped pattern (Fig. 1b). Therefore, it is likely that volcanism and mineralization occurred in a single geodynamic setting. We suggest that late Early Cretaceous volcanic activity in the northern Great Hinggan Range was spatially and temporally coupled with the epithermal mineralization and that the processes shared a common geodynamic setting. Mineralization occurred in an extensional environment towards the end of volcanism and was genetically linked to the closure of the Mongol–Okhotsk Ocean and subduction of the Paleo-Pacific oceanic plate. Assembly of the CAOB was completed by the early Mesozoic (Tang et al. 2013; Zhi et al. 2016), so reactivation of older suture zones, such as those of the Mongolian–Okhotsk Ocean, by subduction of the Paleo-Pacific Plate was likely to have influenced the spatial distribution of the volcanism and ore deposits (Chang and Li 2015; Li et al. 2016).

The Paleo-Pacific Plate subducted to the west from the Early Jurassic onwards and induced extensive island arc magmatism in northeast China. During the Early Cretaceous, the subduction direction changed from NW- to NNW-directed (Goldfarb et al. 2007; Niu et al. 2015). The

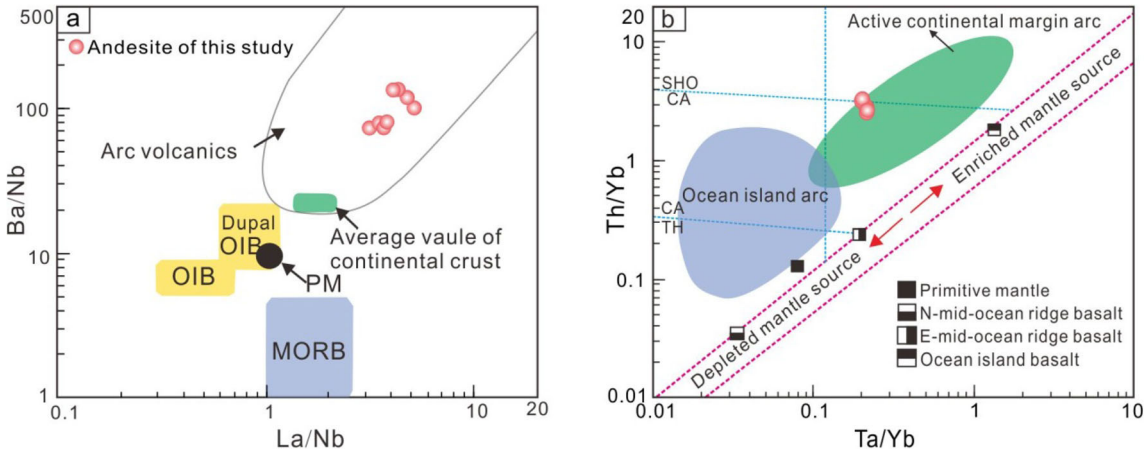

Fig. 12 **a** Ba/Nb versus La/Nb classification diagram (after Jahn et al. 1999); **b** Ta/Yb versus Th/Yb (after Pearce 2008) tectonic discrimination diagrams for the andesites of Longjiang Formation in Sandaowanzi gold deposit

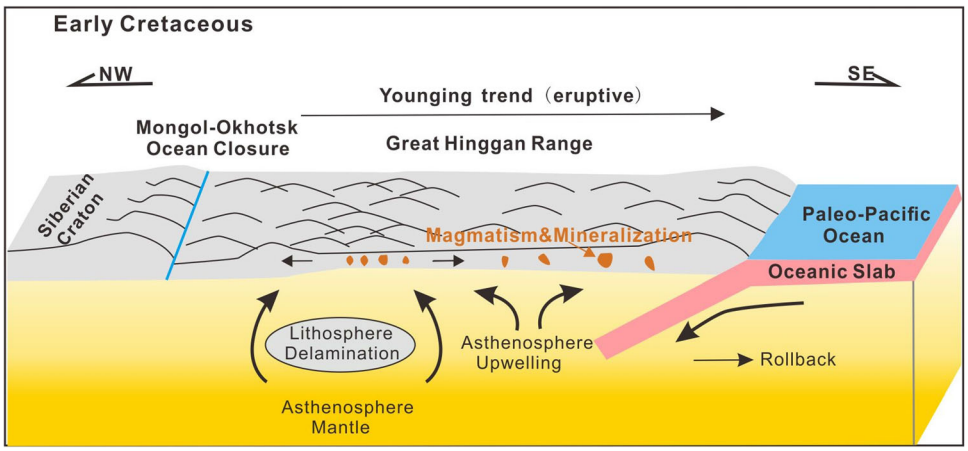

Fig. 13 Schematic model of the Early Cretaceous geodynamic evolution and associated ore deposits in the North Great Hingan Range

change in subduction direction caused a prolonged period of extension, such that the Pacific margin and associated continental magmatic back-arc were in an extensional setting during the late Early Cretaceous (Zhai and Liu 2014; Song 2015; Niu and Tang 2016). Meanwhile, the Mongol–Okhotsk Ocean was closed, causing the northern Great Hinggan Range was in a post-orogenic extensional environment (Fan et al. 2003; Meng 2003; Yang et al. 2015; Deng et al. 2018). This extension was associated with lithospheric thinning, upwelling of the new asthenospheric mantle, and an increased geothermal gradient. Metasomatism added the products of low degree melting to the lithospheric mantle and these, combined with decompression, induced melting. The eruptions occurred close to deep faults, leading to the formation of volcanic fault basins. Once the formation of the volcanic basins was complete, homologous magma was emplaced into the shallow crust, where it provided the heat, metals, and ore-forming fluid that drove the large-scale, epithermal telluride gold polymetallic mineralization that formed the late Early Cretaceous ore deposits of the northern Great Hinggan Range, such as the Sandaowanzi telluride gold deposit (Fig. 13).

8 Conclusions

(1) The andesites of Longjiang Formation are potassium-rich and calc-alkaline series and were derived from partial melting of enriched mantle wedge metasomatized by subducted-slab-derived fluids. These rocks formed in an extensional environment associated with subduction of the oceanic crust of the Pacific Plate.

(2) The U–Pb data yielded a weighted-mean age of the andesites is 123.3 ± 0.8 Ma, close to the mineralization age (119.1 ± 3.9 Ma). It can be considered that the mineralization occurred towards the end of volcanism, and the magmatic activity and mineralization are products of the same geodynamic setting.

(3) The late Early Cretaceous volcanic edifices composed of high-potassium calc-alkaline volcanic rocks are the main targets for the prospecting of epithermal deposits in the northern Great Hinggan Range.

Acknowledgements This work was funded by the National Natural Science Foundation of China (No. 41272093), Natural Science Foundation of Jilin Province (No. 20180101089JC), Key Projects of Science and Technology Development Plan of Jilin Province (No. 20100445).

References

Andersen T (2002) Correction of common lead in U-Pb analyses that do not report ^{204}Pb. Chem Geol 192(1–2):59–79

Arculus RJ (1994) Aspects of magma genesis in arcs. Lithos 33:189–208

Atherton MP, Petford N (1993) Generation of sodium-rich magmas from newly underplated basaltic crust. Nature 362:144–146

Blichert-Toft J, Gleason JD, Télouk P, Albarède F (1999) The Lu–Hf isotope geochemistry of shergottites and the evolution of the Martian mantle–crust system. Earth Planet Sci Lett 173:25–39

Boynton WV (1984) Cosmochemistry of the rare earth elements: meteorite studies. In: Henderson P (ed) Rare earth elements geochemistry. Elsevier, Amsterdam, pp 63–114

Chang JJ, Li BL (2015) Geochemistry, U–Pb geochronology, and Hf isotopic characteristics and geological significance of the tuff from Dong'an Gold Deposit, Lesser Khingan Mountains, NE China. Conserv Util Miner Resour 6:12–21 (**(in Chinese with English abstract)**)

Chen YJ (2010) On epizonogenism and genetic classification of hydrothermal deposits. Earth Sci Front 17:27–34 (**(in Chinese with English abstract)**)

Chen GW, Xia B, Xiao ZY, Yu HX, Wang H, Zhong ZH, Wang GQ (2001) Characteristics of epithermal deposits and the prospecting guide in China. Geol Resour 10:165–171 (**(in Chinese with English abstract)**)

Ciobanu CL, Cook NJ, Spry PG (2006) Preface-Special issue: telluride and selenide minerals in gold deposits-how and why? Miner Petro 87:163–169

Condie KC (2015) Mantle plumes and their record in earth history. Cambridge University Press, London

Cook NJ, Ciobanu CL (2005) Mineral deposit research: meeting the global challenge. In: Mao JW, Bierlein FP (eds) Tellurides in Au deposits: implications for modelling. Springer, Berlin, pp 63–114

Cook NJ, Ciobanu CL, Spry P, Voudouris P (2009) Understanding gold–(silver)–telluride–(selenide) mineral deposits. Episodes 32:249–263

Cooke DR (2001) Epithermal Au–Ag–Te mineralization, Acupan, Baguio District, Philippines: numerical simulations of mineral deposition. Econ Geol 96:109–131

Cooke DR, Simmons SF (2000) Characteristics and genesis of epithermal gold deposits. Rev Econ Geol 13:221–244

Damdinov BB, Mironov AG, Borovikov AA, Guntypov BB, Karmanov NS, Borisenko AS, Garmaev BL (2007) Composition and conditions of formation of gold-telluride mineralization in the Tissa-Sarkhoi gold-bearing province (East Sayan). Russ Geol Geophys 48:643–655

Deng CZ, Sun DY, Ping XQ, Huang H, Zhang LD, Lu S (2018) Geochemistry of early cretaceous volcanic rocks in the Northeastern Great Xing'an Range, northeast China and implication for geodynamic setting. Int Geol Rev. https://doi.org/10.1080/00206814.2018.1528481

Deng CZ, Sun DY, Han JS, Li GH, Feng YZ, Xiao B, Li RC, Shi HL, Xu GZ, Yang D (2019) Ages and petrogenesis of the Late Mesozoic igneous rocks associated with the Xiaokele porphyry Cu–Mo deposit, NE China and their geodynamic implications. Ore Geol Rev 107:417–433

Fan WM, Guo F, Wang YJ, Lin G (2003) Late Mesozoic calc-alkaline volcanism of post-orogenic extension in the northern Da Hinggan Mountains, northeastern China. J Volcanol Geotherm Res 121:115–135

Gao S, Xu H, Zang YQ, Wang T (2018) Mineralogy, ore-forming fluids and geochronology of the Shangmachang and Beidagou gold deposits, Heilongjiang province, NE China. J Geochem Explor 188:137–155

Ge WC, Lin Q, Sun DY, Wu FY, Yuan ZK, Li WY, Chen MZ, Yin CX (1999) Geochemical characteristics of the Mesozoic basalts in Da Hinggan Ling: evidence of the mantle-crust interaction. Acta Petrol Sin 15:396–407 (**(in Chinese with English abstract)**)

Ge WC, Lin Q, Sun DY, Wu FY, Li XH (2000) Geochemical research into origins of two types of Mesozoic rhyolites in Daxing'anling. Earth Sci 25:173–178 (**(in Chinese with English abstract)**)

Ge WC, Wu FY, Zhou CY, Abdel Rahman AA, Naulet N (2005) Emplacement age of the Tahe granite and its constraints on the tectonic nature of the Ergun block in the northern part of the Da Hinggan Range. Chin Sci Bull 50:2097–2105

Gill JB (1981) Orogenic andesites and plate tectonics. Springer, New York

Goldfarb RJ, Hart C, Davis G, Groves D (2007) East Asian gold: deciphering the anomaly of Phanerozoic gold in Precambrian cratons. Econ Geol 102:341–345

Green TH (1995) Significance of Nb/Ta as an indicator of geochemical processes in the crust-mantle system. Chem Geol 120:347–359

Griffin WL, Wang X, Jackson SE, Pearson NJ, O'Reilly SY, Xu X, Zhou X (2002) Zircon chemistry and magma mixing, SE China: in-situ analysis of Hf isotopes, Tonglu and Pingtan igneous complexes. Lithos 61:237–269

Grove TL, Kinzler RJ (1986) Petrogenesis of andesites. Annu Rev Earth Planet Sci 14:417–454

Halim N, Kravchinsky V, Gilder S, Cogne J, Alexutin M, Sorokin A, Courtillot V, Chen Y (1998) A palaeomagnetic study from the Mongol–Okhotsk region: rotated Early Cretaceous volcanics and remagnetized Mesozoic sediments. Earth Planet Sci Lett 159:133–145

Hastie AR, Kerr AR, Pearce JA, Mitchell SF (2007) Classification of altered volcanic island arc rocks using immobile trace elements: development of the Th–Co discrimination diagram. J Petrol 48:2341–2357

Hawkesworth CJ, Hergt JM, Ellam RM, McDermott F (1991) Element fluxes associated with subduction related magmatism. Philos Trans R Soc Lond Ser A 335:393–405

Hofmann AW, Jochum KP, Seufert M, White WM (1986) Nb and Pb in oceanic basalts: new constraints on mantle evolution. Earth Planet Sci Lett 79(1–2):33–45

Hoskin PWO, Schaltegger U (2003) The composition of zircon and igneous and metamorphic petrogenesis. Rev Miner Geochem 53:27–62

Huang JL, Zhao DP (2006) High-resolution mantle tomography of China and surrounding regions. J Geophys Res 111:B9

Ionov DA, Grégoire M, Prikhod'ko VS (1999) Feldspar–Ti-oxide metasomatism in off-cratonic continental and oceanic upper mantle. Earth Planet Sci Lett 165:37–44

Jahn BM, Wu FY, Capdevila R, Martineau F, Zhao ZH, Wang YX (2001) Highly evolved juvenile granites with tetrad REE patterns: the Woduhe and Baerzhe granites from the Great Xing'an Mountains in NE China. Lithos 59:171–198

Jahn BM, Wu FY, Lo CH, Tsai CH (1999) Crust–mantle interaction induced by deep subduction of the continental crust: geochemical and Sr–Nd isotopic evidence from post-collisional mafic–ultramafic intrusions of the northern Dabie complex, central China. Chem Geol 157:119–146

Ji Z, Meng QA, Wang CB, Ge WC, Yang H, Zhang YL, Dong Y, Jin X (2019) Early Cretaceous adakitic lavas and A-type rhyolites in the Songliao Basin, NE China: implications for the mechanism of lithospheric extension. Gondwana Res 71:28–48

Kazimoto EO, Ikingura JR (2014) Trace element geochemistry and petrogenesis of the granitoids and high-K andesite hosting gold mineralisation in the Archean Musoma-Mara Greenstone Belt, Tanzania. J Afr Earth Sci 91:66–78

Kelley KD, Ludington S (2002) Cripple Creek and other alkaline-related gold deposits in the southern Rocky Mountains, USA: influence of regional tectonics. Miner Deposita 37:38–60

Kirchenbaur M, Münker C, Schuth S, Garbe-Schönberg D, Marchev P (2012) Tectonomagmatic constraints on the sources of Eastern Mediterranean K-rich lavas. J Petrol 53:27–65

Li JY (2006) Permian geodynamic setting of Northeast China and adjacent regions: closure of the Paleo-Asian Ocean and subduction of the Paleo-Pacific Plate. J Asian Earth Sci 26:207–224

Li JY, Gao XY, Bian XF, Chen SW, Ding QH (2013) LA–ICP–MS zircon U–Pb dating and geochemical characteristics of the Mesozoic volcanic rocks from Longjiang basin in northern Da Hinggan Mountains and their geological implications. Geol Bull China 32:1195–1211 (**in Chinese with English abstract**)

Li BL, Sun YG, Chen GJ, Xi AH, Zhi YB, Chang JJ, Peng B (2016) Zircon U–Pb geochronology, geochemistry and Hf isotopic composition and its geological implication of the fine-grained syenogranite in Dong'an Goldfield from the Lesser Xing'an Mountains. Earth Sci 41:3–16 (**in Chinese with English abstract**)

Lin Q, Ge WC, Sun DY, Wu FY, Chong KW, Kyung DM, Myung SJ, MoonW CSK, Sung HY (1998) Tectonic implications of Mesozoic volcanic rocks in Northeastern China. Sci Geol Sin 33:129–139 (**in Chinese with English abstract**)

Liu JL, Davis GA, Lin ZY, Wu FY (2005) The Liaonan metamorphic core complex, Southeastern Liaoning Province, North China: a likely contributor to Cretaceous rotation of Eastern Liaoning, Korea and contiguous areas. Tectonophysics 407:65–80

Liu JL, Bai XD, Zhao SJ, Tran MD, Zhang ZC, Zhao ZD, Zhao HB, Lu J (2011) Geology of the Sandaowanzi telluride gold deposit of the northern Great Xing'an Range, NE China: geochronology and tectonic controls. J Asian Earth Sci 41:107–118

Liu J, Wu G, Huang QN, Gao DZ, Yang XS (2013a) $^{40}Ar/^{39}Ar$ dating of gold-bearing quartz vein from the Shabaosi gold deposit at the Northern end of the Great Xing'an Range and its tectonic significance. Acta Geol Sin 87:1571–1579 (**n Chinese with English abstract**)

Liu JL, Zhao SJ, Cook NJ, Bai XD, Zhang ZC, Zhao ZD, Zhao HB, Lu J (2013b) Bonanza-grade accumulations of gold tellurides in the Early Cretaceous Sandaowanzi deposit, northeast China. Ore Geol Rev 54:110–126

Liu WL, Huang QT, Gu M, Zhong Y, Zhou RJ, Gu XD, Zheng H, Liu JN, Lu XX, Xia B (2018) Origin and tectonic implications of the Shiquanhe high-Mg andesite, western Bangong suture. Tibet Gondwana Res 60:1–14

Liu Y, Chu XL, Sun JG, Han JL, Ren L, Gu A, Zhao KQ (2020) Early Cretaceous bimodal magmatism related epithermal mineralization: a case study of the Gaosongshan gold deposit in the northern Lesser Xing'an Range NE China. Ore Geol Rev 121:103563

Ludwig KR (2003) User's manual for Isoplot 3.6: a geochronological toolkit for microsoft excel. Berkeley Geochronology Center, California, USA

Lü J (2011) The geologic characteristics, minerogenetic conditions and deposit model of the Sandaowanzi gold deposit, Heihe City, Helongjing Province. Ph.D. Thesis, China University of Geosciences, Beijing (**in Chinese with English abstract)**

Ma XH, Gao R, Zhou ZH, Zhu WP (2015) Early Cretaceous high-Mg diorites in the Yanji area, northeastern China: petrogenesis and tectonic implications. J Asian Earth Sci 97:393–405

Mao JW, Li XF, Zhang ZH, Wang YT, Hu HB (2003) Geology, distribution, types and tectonic settings of Mesozoic epithermal gold deposits in East China. Geol J China Univ 9:620–637 (**in Chinese with English abstract**)

Meng QR (2003) What drove late Mesozoic extension of the northern China-Mongolia tract? Tectonophysics 369:155–174

Niu YL, Tang J (2016) Origin of the Yellow Sea: an insight. Sci Bull 61:1076–1080

Niu YL, Liu Y, Xue QQ, Shao FL, Chen S, Duan M, Guo PY, Gong HM, Hu Y, Hu ZX, Kong JJ, Li JY, Liu JJ, Sun P, Sun WL, Ye L, Xiao YY, Zhang Y (2015) Exotic origin of the Chinese continental shelf: new insights into the tectonic evolution of the western Pacific and eastern China since the Mesozoic. Sci Bull 60:1598–1616

Ouyang HG, Mao JW, Santosh M, Zhou J, Zhou ZH, Wu Y, Hou L (2013) Geodynamic setting of Mesozoic magmatism in NE China and surrounding regions: perspectives from spatio-temporal distribution patterns of ore deposits. J Asian Earth Sci 78:222–236

Pals DW, Spry PG (2003) Telluride mineralogy of the low-sulfidation epithermal Emperor gold deposit, Vatukoula, Fiji. Miner Petrol 79:285–307

Pearce JA (2008) Geochemical fingerprinting of oceanic basalts with applications to ophiolite lassification and the search for Archean oceanic crust. Lithos 100:14–48

Pearce JA, Parkinson IJ (1993) Trace element models for mantle melting: application to volcanic arc petrogenesis. Geol Soc Lond Spec Publ 76:373–403

Pearce JA, Peate DW (1995) Tectonic implications of the composition of volcanic ARC magmas. Annu Rev Earth Planet Sci 23:251–285

Polat A, Hofmann AW, Rosing MT (2002) Boninite-like volcanic rocks in the 3.7–3.8 Ga Isua greenstonebelt, West Greenland: geochemical evidence for intra-oceanic subduction zone processes in the early Earth. Chem Geol 184:231–254

Qiu YZ, Tu QC, Berger BR (2008) Epithermal gold deposits of China. Geochimica 37:329–343

Quan YK, Yang DB, Mu MS, Hao LR, Yang HT, Wang AQ, Xu WL (2020) Tectonic evolution of the northeastern North China Craton: constraints from geochronology and Sr–Nd–Hf–O isotopic data from Late Triassic intrusive rocks on Liaodong Peninsula NE China. Lithos 362–363:105489

Rapp RP, Watson EB (1995) Dehydration melting of metabasalt at 8–32 kbar: implications for continental growth and crust–mantle recycling. J Petrol 36(4):891–931

Richards JP (2009) Postsubduction porphyry Cu–Au and epithermal Au deposits: products of remelting of subduction-modified lithosphere. Geology 37:247–250

Rudnick RL, Gao S, Ling WL, Liu YS, McDonough WF (2004) Petrology and geochemistry of spinel peridotite xenoliths from Hannuoba and Qixia, North China craton. Lithos 77:609–637

Schiano P, Eiler JM, Hutcheon ID, Stolper EM (2000) Primitive CaO-rich, silica-undersaturated melts in island arcs: evidence for the

involvement of clinopyroxene-rich lithologies in the petrogenesis of arc magmas. Geochem Geophys Geosyst 1:1525–2027

Schiano P, Monzier M, Eissen JP, Martin H, Koga KT (2010) Simple mixing as the major control of the evolution of volcanic suites in the Ecuadorian Andes. Contr Miner Petrol 160(2):297–312

Shao S (2017) The characteristics and Significance of early cretaceous volcanic rocks in Heihe area. Ph.D. Thesis, China University of Geosciences, Beijing (**in Chinese with English abstract)**

Sillitoe RH (1997) Characteristics and controls of the largest porphyry copper-gold and epithermal gold deposits in the circum-Pacific region. Aust J Earth Sci 44:73–388

Song SG (2015) Exotic origin of the Chinese continental shelf. Sci Bull 60:1625–1625

Sun SS, McDonough WF (1989) Chemical and isotopic systematics of oceanic basalts: implications for mantle composition and processes. In: Saunders AD, Norry MJ (eds) Magmatism in the Ocean Basins, vol 42. Geological Society of London, London, pp 313–345

Sun GZ, Liu SW, Wang MJ, Bao H, Teng GX (2020) Complex Neoarchean mantle metasomatism: evidence from sanukitoid diorites-monzodiorites-granodiorites in the northeastern North China Craton. Precambrian Res 342:105692

Tang GJ, Wang Q, Zhao ZH, Wyman DA, Chen HH, Jia XH, Jiang ZQ (2009) LA–ICP–MS zircon U–Pb geochronology, element geochemistry and petrogenesis of theandesites in the eastern Taerbieke gold deposit of the western Tianshan region. Acta Petrol Sin 25(6):1341–1352

Tang J, Xu WL, Wang F, Wang W, Xu MJ, Zhang YH (2013) Geochronology and geochemistry of Neoproterozoic magmatism in the Erguna Massif, NE China: petrogenesis and implications for the breakup of the Rodinia supercontinent. Precambrian Res 224:597–611

Tatsumi Y, Hamilton DL, Nesbitt RW (1986) Chemical characteristics of fluid phase released from a subducted lithosphere and origin of arc magmas: evidence from high-pressure experiments and natural rocks. J Volcanol Geotherm Res 29:293–309

Taylor SR, McLennan S (1995) The geochemical evolution of the continental crust. Rev Geophys 33(2):241–265

Tomurtogoo O, Windley BF, Kroner A, Badarch G, Liu DY (2005) Zircon age and occurrence of the Adaatsag ophiolite and Muron shear zone, central Mongolia: constraints on the evolution of the Mongol–Okhotsk ocean, suture and orogen. J Geol Soc 162:125–134

Wallier S, Rey R, Kouzmanov K, Pettke T (2006) Magmatic fluids in the Breccia-hosted epithermal Au–Ag deposit of Roşia Montană, Romania. Econ Geol 101:923–954

Wang F, Zhou XH, Zhang LC, Ying JF, Zhang YT, Wu FY, Zhu RX (2006) Late Mesozoic volcanism in the Great Xing'an Range (NE China): Timing and implications for the dynamic setting of NE Asia. Earth Planet Sci Lett 251:179–198

Wang SS, Liu JY, Ji HW, Lü J, Zhou S, Liu JL (2017) Geochronology and geochemistry of the andesites of Longjiang Formation in the Sandaowanzi gold deposit, Heilongjiang Province. Acta Petrol Sin 33:2604–2618 ((**in Chinese with English abstract)**)

Wiedenbeck M, Alle P, Corfu F, Griffin WL, Meier M, Oberli F, Quadt AV, Roddick JC, Spiegel W (1995) Three natural zircon standards for U–Th–Pb, Lu–Hf, trace element and REE analyses. Geostand Geoanal Res 19:1–23

Wu FY, Sun DY, Li BM, Jahn BM, Wilde S (2002) A-type granites in Northeastern China: age and geochemical constraints on their petrogenesis. Chem Geol 187:143–173

Wu FY, Yang YH, Xie LW, Yang JH, Xu P (2006) Hf isotopic compositions of the standard zircons and baddeleyites used in U/Pb geochronology. Chem Geol 234:105–126

Wu FY, Li XH, Zheng YF, Gao S (2007) Lu-Hf isotopic systematics and their applications in petrology. Acta Petrol Sin 23:185–220 (**in Chinese with English abstract**)

Xu WL, Pei FP, Wang F, Meng E, Ji WQ, Yang DB, Wang W (2013) Spatial–temporal relationships of Mesozoic volcanic rocks in NE China: constraints on tectonic overprinting and transformations between multiple tectonic regimes. J Asian Earth Sci 74:167–193

Yang JH, Wu FY, Shao JA, Wilde SA, Xie LW, Liu XM (2006) Constrains on the timing of uplift of the Yanshan Fold and Thrust Belt, North China. Earth Planet Sci Lett 246(3–4):336–352

Yang JH, Wu FY, Chung SL, Lo CH, Wilde SA, Davis GA (2007) Rapid exhumation and cooling of the Liaonan metamorphic core complex: inferences from $^{40}Ar/^{39}Ar$ thermochronology and implications for Late Mesozoic extension in the eastern North China Craton. Geol Soc Am Bull 119:1405–1414

Yang H, Ge WC, Zhao GC, Dong Y, Bi JH, Wang ZH, Yu JJ, Zhang YL (2014) Geochronology and geochemistry of Late Pan-African intrusive rocks in the Jiamusi-Khanka Block, NE China: petrogenesis and geodynamic implications. Lithos 208–209:220–236

Yang YT, Guo ZX, Song CC, Li XB, He S (2015) A short-lived but significant Mongol–Okhotsk collisional orogeny in latest Jurassic-earliest Cretaceous. Gondwana Res 28:1096–1116

Yang Q, Ren YS, Hao YJ, Wang B, Sun ZM, Li JM (2019) Ore fluid, geochronology and tectonic setting of mesothermal gold metallogeny in southeastern Jilin Province, Northeast China: a case study of the Shajingou gold deposit. Ore Geol Rev 109:229–252

Ying HL (1999) The global background of epithermal gold deposits. J Precious Met Geol 8:241–250 (**in Chinese with English abstract**)

Yuan HL, Gao S, Liu XM, Li HM, Detlef G, Wu FY (2004) Accurate U–Pb age and trace element determinations of zircon by laser ablation-inductively coupled plasma–mass spectrometry. Geostand Geoanal Res 28:353–370

Yuan C, Sun M, Xiao WJ, Wilde S, Li XH, Liu XH, Long XP, Xia XP, Ye K, Li JL (2009) Garnet-bearing tonalitic porphyry from East Kunlun, Northeast Tibetan Plateau: implications for adakite and magmas from the MASH zone. Int J Earth Sci 98:1489–1510

Zeng QD, Guo F, Zhou L, Duan XX (2016) Two periods of mineralization in Xiaoxinancha Au–Cu deposit, NE China: evidences from the geology and geochronology. Geol J 51:51–64

Zhai DG, Liu JJ (2014) Gold–telluride–sulfide association in the Sandaowanzi epithermal Au–Ag–Te deposit, NE China: implications for phase equilibrium and physicochemical conditions. Miner Petrol 108:853–871

Zhai DG, Liu JL, Ripley EM, Wang JP, Tian SH (2015) Geochronological and He–Ar–S isotopic constraints on the origin of the Sandaowanzi gold–telluride deposit, northeastern China. Lithos 212–215:338–352

Zhai DG, Williams-Jones AE, Liu JL, Tombros JSF, Cook NJ (2018) Mineralogical, fluid inclusion, and multiple isotope (H–O–S–Pb) Constraints on the Genesis of the Sandaowanzi Epithermal Au–Ag–Te Deposit, NE China. Econ Geol 113:1359–1382

Zhang KJ (2014) Genesis of the Late Mesozoic Great Xing'an Range Large Igneous Province: a Mongol–Okhotsk slab window model. Int Geol Rev 56:1557–1583

Zhang JH, Ge WC, Wu FY, Wilde SA, Yang JH, Liu XM (2008) Large-scale Early Cretaceous volcanic events in the northern Great Xing'an Range, Northeastern China. Lithos 102:138–157

Zhang JH, Gao S, Ge WC, Wu FY, Yang JH, Wilde SA, Li M (2010) Geochronology of the Mesozoic volcanic rocks in the Great Xing'an Range, northeastern China: implications for subduction-induced delamination. Chem Geol 276:144–165

Zhang YT, Sun FY, Wang S, Wei X (2018) Geochronology and geochemistry of Late Jurassic to Early Cretaceous granitoids in the northern Great Xing'an Range, NE China: petrogenesis and implications for late Mesozoic tectonic evolution. Lithos 312–313:171–185

Zhang KJ, Yan LL, Ji C (2019) Switch of NE Asia from extension to contraction at the mid-Cretaceous: a tale of the Okhotsk oceanic plateau from initiation by the Perm Anomaly to extrusion in the Mongol–Okhotsk ocean? Earth Sci Rev 198:102941

Zhao HL, Deng JF, Chen FJ, Hu Q, Zhao SK (1998) Petrology of the Mesozoic volcanic rocks and the basin formation in the Northeast China. Geoscience 12:57–63 (**in Chinese with English abstract**)

Zhi YB, Li BL, Xi AH, Xu QL, Zhang L, Sun YG, Chang JJ, Peng B (2016) Geochronology and geochemistry of the major host rock of the Dong'an gold deposit, Lesser Khingan Range: implications for petrogenesis and metallogenic setting during the Early-Middle Jurassic in northeast China. Chem Erde 76:257–274

Zhou CF, Wang XZ, Li XW, Yang HB, Song GB, Duan MX, Guo HY (2018) Mesozoic intrusive rocks and their constraints on mineralization in Baoxinggou gold deposit in Tahe County, Heilongjiang Province. Miner Depos 37:137–150 (**in Chinese with English abstract**)

Zorin YA (2016) Geodynamics of the western part of the Mongolia–Okhotsk collisional belt, Trans-Baikal region (Russia) and Mongolia. Tectonophysics 306:33–56

Zou XT (2015) Geological, geochemical characteristics and ore-prospecting of the I $^{\#}$Ore Vein in Ciweigou Gold Deposit, Yanbian Area. Master's Thesis, Jilin University, Changchun (**in Chinese with English abstract**)